FEATURE EXTRACTION FROM RAILROAD BEARING ONBOARD VIBRATION SENSORS USING MACHINE LEARNING MODELS

A Thesis

by

DIEGO CANTU

Submitted in Partial Fulfillment of the

Requirements for the Degree of

MASTER OF SCIENCE IN ENGINEERING

Major Subject: Mechanical Engineering

The University of Texas Rio Grande Valley
December 2025

FEATURE EXTRACTION FROM RAILROAD BEARING

ONBOARD VIBRATION SENSORS USING

MACHINE LEARNING MODELS

A Thesis
by
DIEGO CANTU

COMMITTEE MEMBERS

Dr. Constantine Tarawneh
Chair of Committee

Dr. Ping Xu
Co-Chair of Committee

Dr. Heinrich Foltz
Committee Member

Dr. Arturo Fuentes
Committee Member

December 2025

ABSTRACT

Cantu, Diego, Feature Extraction from Railroad Bearing Onboard Vibration Sensors using Machine Learning Models. Master of Science in Engineering (MSE), December 2025, 59 pp., 24 tables, 21 figures, 17 references.

The University Transportation Center for Railway Safety (UTCRS) has developed an algorithm capable of identifying defective railroad bearings, determining damaged component(s) within, and quantifying severity of the defects. The defect-detection algorithm requires the operating speed as an input, which is not readily available in field operation of onboard sensors. Therefore, onboard sensors deployed in rail revenue service must rely on Global Positioning Systems (GPS) to obtain speed, which can be power-intensive and susceptible to signal interference. This study covers the development of a vibration-based model that extracts operating speed from wireless sensor data to enable fully autonomous onboard diagnostics. Signal filtering and envelope-analysis are applied to extract the fundamental defect frequency and its harmonics. The K-Means clustering machine learning algorithm then estimates the rotational speed across multiple filter-envelope combinations. The resulting model produces reliable speed extraction, supporting real-time integration of the UTCRS bearing health monitoring algorithm in field service conditions.

DEDICATION

I dedicate the completion of my master’s to my family, friends, and professors. Mom, Aracely Cantu, you are the backbone of everything I do. Dad, Octavio Cantu, your work continues to inspire me to become a better version of myself. To my siblings, Aracely Cantu, Ivan Cantu, and Mauricio Cantu, thank you for your constant support. I owe this achievement to all of you.

ACKNOWLEDGEMENTS

I would like to express my deepest gratitude to Dr. Constantine Tarawneh and Dr. Ping Xu, whose guidance and mentorship have illuminated my journey from start to finish. Dr. Tarawneh, thank you for pushing me and molding me into something greater than I could have imagined. Your restless efforts and commitment to students are truly inspiring. I am grateful to you for always believing in me and for pushing me to pursue the opportunity you presented. Because of your efforts and those of the rest of my committee, I can say I have grown not only as a researcher but also as an engineer and a person. I would like to express my gratitude to the NSF CREST Center for Multidisciplinary Research Excellence in Cyber-Physical Infrastructure Systems (CREST-MECIS) for their financial support through the NSF Award No. 2112650. I would also like to acknowledge the University Transportation Center for Railway Safety (UTCRS) for providing access to all the data sets needed to complete this study.

TABLE OF CONTENTS

Page

ABSTRACT III

DEDICATION IV

ACKNOWLEDGEMENTS 6

TABLE OF CONTENTS VI

LIST OF TABLES IX

LIST OF FIGURES XI

CHAPTER I 1

1.1 INTRODUCTION 1

1.2 TAPERED ROLLER BEARINGS OVERVIEW 1

1.2.1 Basic Structure Function 2

1.2.2 Bearing Specifications and Classes 2

1.2.3 Bearing Defects in Railway Systems 3

1.3 CURRENT MAINTENANCE SYSTEMS 4

1.3.1 Hot Bearing Detectors (HBDs) 4

1.3.2 Acoustic Bearing Detectors (ABDs) and Track Acoustic Detector Systems (TADS™) 6

1.3.3 Wheel Impact Load Detectors (WILDs) 7

1.4 ONBOARD WIRELESS CONDITION MONITORING SYSTEMS 8

1.4.1 UTCRS Wireless Sensor System 9

1.5 RELATED WORK 10

1.6 MOTIVATION 12

CHAPTER II 16

2.1 MACHINE LEARNING BACKGROUND 16

2.1.1 Supervised Learning 16

2.1.2 Unsupervised Learning 16

2.1.3 K-Means Clustering 17

2.2 ALGORITHM PERFORMANCE AND SCORING SYSTEMS 18

2.2.1 Error Scoring Methodology 19

2.3 CONFIDENCE SCORE METHODS 21

2.3.1 RMS-Based Consensus Scoring Method 21

2.3.2 Defect Energy Based Confidence Scoring Method 23

CHAPTER III 24

3.1 FEATURE EXTRACTION FRAMEWORK 24

3.1.1 Data and Signal Processing 25

3.1.2 Denoising Techniques 26

3.1.3 Envelope Extraction 29

3.1.4 Speed Extraction 32

CHAPTER IV 35

4.1 UTCRS LABORATORY OVERVIEW 35

4.2 BEARING TEST RIGS 37

4.3 INSTRUMENTATION 38

4.4 Software and Computational Environment 39

CHAPTER V 40

5.1 Validation Experiments and Operating Conditions 40

5.2 Aggregate Algorithm Performance 40

5.3 Results for Bearing with a Defective Cone (Exp. 181A) 42

5.3.1 Low-Speed Conditions (234 rpm and 327 rpm) 42

5.3.2 Mid-Speed Conditions (420 rpm and 560 rpm) 44

5.3.3 High-Speed Conditions (618 rpm and 700 rpm) 45

5.3.4 Comparison Across Speed Ranges 47

5.4 Results for Bearings with a Defective Cup (Exp. 177R) 47

5.4.1 Low-Speed Conditions (234 rpm and 327 rpm) 47

5.4.2 Mid-Speed Conditions (420 rpm and 560 rpm) 49

5.4.3 High-Speed Conditions (618 rpm and 700 rpm) 50

5.4.4 Comparison Across Speed Ranges 51

5.5 Reliability Analysis of Speed Estimation for Early Defect Detection 51

CHAPTER VI 54

REFERENCES 56

APPENDIX 59

VITA 61

LIST OF TABLES

Table 1: AAR class F and K bearing dimensions and load capacities [5] 3

Table 2: Common testing axle speeds and equivalent track speeds.. 37

Table 3: Aggregate performance across all experiments and cases 41

Table 4: Algorithm aggregate performance at low-speed conditions (Exp. 181A) 43

Table 5: Low-speed results at 17% load (Exp. 181A) 43

Table 6: Low-speed results at 100% load (Exp. 181A) 43

Table 7: Algorithm aggregate performance at mid-speed conditions (Exp. 181A) 44

Table 8: Mid-speed results at 17% load (Exp. 181A) 44

Table 9: Mid-speed results at 100% load (Exp. 181A) 45

Table 10: Algorithm aggregate performance at high-speed conditions (Exp. 181A) 46

Table 11: High-speed results at 17% load (Exp. 181A)... 46

Table 12: High-speed results at 100% load (Exp. 181A)... 46

Table 13: Algorithm aggregate performance at low-speed conditions (Exp. 177R).................... 48

Table 14: Low-speed results at 17% load (Exp. 177R) 48

Table 15: Low-speed results at 100% load (Exp. 177R) 48

Table 16: Algorithm aggregate performance at mid-speed conditions (Exp. 177R) 49

Table 17: Mid-speed results at 17% load (Exp. 177R) 49

Table 18: Mid-speed results at 100% load (Exp. 177R) 49

Table 19: Algorithm aggregate performance at high-speed conditions (Exp. 177R).................. 50

Table 20: High-speed results at 17% load (Exp. 177R)... 50

Table 21: High-speed results at 100% load (Exp. 177R) 51

Table 22: Probability of early detection for cone defective bearings (Exp. 181A) 52

Table 23: Probability of early detection for cup defective bearings (Exp. 177R) 53

Table 24: Confidence-error correlations using Pearson correlation values 60

LIST OF FIGURES

Figure 1: Exploded view of a railroad tapered roller bearing assembly [6]. 2

Figure 2: Localized bearing defects (pitting and spalling). 4

Figure 3: Water-etched bearing defect. 4

Figure 4: Hot Bearing Detector (HBD) diagram [7].. 5

Figure 5: Track Acoustic Detector System (TADS™) at rail side [1]. 7

Figure 6: Wheel Impact Load Detectors (WILD) field installation.. 8

Figure 7: UTCRS wireless onboard sensor [8]. 10

Figure 8: Flowchart of the optimized railroad bearing defect-detection algorithm [10]. 13

Figure 9: K-Means Clustering [13]... 17

Figure 10: Feature Extraction Methodology Framework. 24

Figure 11: Normalized raw vibration signal in time and frequency domains.............................. 25

Figure 12: Normalized and low-pass filtered signal of a cone-defective bearing at 234 rpm and 17% load. 26

Figure 13: Normalized and bandpass-filtered signal of a cone-defective bearing at 234 rpm and 17% load. 27

Figure 14: Normalized and wavelet-filtered signal for a cone-defective bearing at 234 rpm and 17% load. 29

Figure 15: Envelope extraction comparison to filtered time-domain signal................................ 30

Figure 16: Hilbert envelope comparison to a filtered signal in the frequency domain................ 31

Figure 17: TEO envelope comparison to a bandpass-filtered signal in the frequency domain. ... 32

Figure 18: Four bearing test axle setup and instrumentation diagram. 36

Figure 19: A) single bearing tester (SBT), and B) four bearing tester (4BT). 36

Figure 20: UTCRS single bearing tester (SBT) features. 38

CHAPTER I

INTRODUCTION AND MOTIVATION

1.1 Introduction

There are approximately 1,000 railway derailments reported to the U.S. Department of Transportation (USDOT) annually, resulting in damage to infrastructure, businesses, and surrounding ecosystems [1]. In February 2023, a Norfolk Southern Railway train derailed thirty-eight mixed freight cars; three of which contained flammable and combustible hazardous materials that were released into the environment. This accident was caused by a bearing overheating and catastrophically failing, which resulted in over a billion dollars in damages and lawsuit settlements, and widespread harm to the adjacent ecosystem [2]. With the railway industry carrying an estimated one-third of U.S. exports and delivering nearly 1.5 billion tons of freight annually, it is crucial to advance preventive measures to facilitate defect detection and mitigate potential catastrophes [3].

This study uses machine learning algorithms to extract features from vibration signatures acquired from onboard sensors mounted on freight railcars with the ultimate goal of implementing proactive condition monitoring algorithms in rail revenue service. The study presented here covers the development and implementation of six filter-envelope combinations that work in tandem to extract speed from vibration signatures of tapered-roller bearings. The extraction of speed enables and promotes early detection of defective bearings through the defect detection framework developed by researchers at the University Transportation Center for Railway Safety (UTCRS).

1.2 Tapered Roller Bearings Overview

A tapered roller bearing is an essential component of the railcar bogie that minimizes friction between a rotating axle and the stationary housing of a freight car, allowing for smooth motion while withstanding harsh operating conditions. According to Association of American Railroads (AAR) suggested guidelines and subsequent Federal Railroad Administration (FRA) regulations, modern freight cars are designed and certified to operate at gross rail loads up to 286,000 lbs., in which they rely heavily on roller bearings to ensure safe and reliable operations [4] [5].

1.2.1 Basic Structure Function

A tapered roller bearing assembly consists of outer ring (cup), inner rings (cones), rollers, cage, spacer ring, wear rings, seals, and lubrication. Tapered roller bearings are widely used in industry due to their ability to support combined loads and handle bidirectional axial forces generated during acceleration. The cone assembly consists of a set of 23 rollers on the cone held in place by a cage. Figure 1 shows the main components that make up a tapered roller bearing.

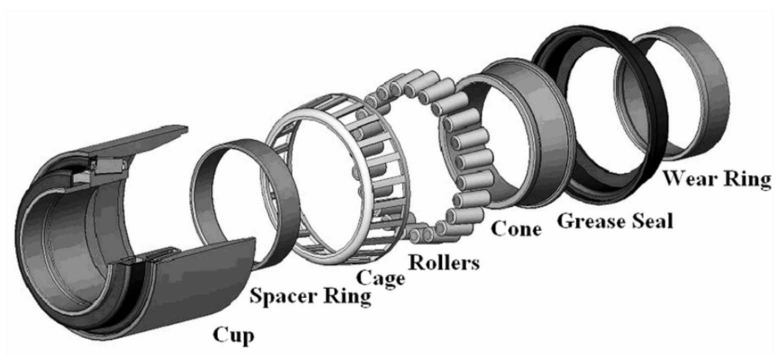

Figure 1: Exploded view of a railroad tapered roller bearing assembly [6].

1.2.2 Bearing Specifications and Classes

According to the Association of American Railroads (AAR), bearings are categorized into classes based on their dimensions. The two most common classes of tapered roller bearings used in the North American freight rail revenue service are class F and class K. Class F and class K bearings both have similar dimensions and load capacities, offering high rigidity and versatility for heavy-duty tasks where durability, load capacity, and efficiency are needed. This study focuses on these two bearing classes as the UTCRS has conducted many tests utilizing class F and K bearings and has collected an extensive library of vibration signatures spanning almost two decades of research. The data was collected using specially designed dynamic bearing test rigs that closely mimic service operating conditions. Table 1 gives the geometries and load capacities of class F and K bearings.

Table 1: AAR class F and K bearing dimensions and load capacities [5]

Class	Size (mm)	Size (in)	Load (kN)	Load (lbf)
Class F	165×305	6.5×12	153	34,400
Class K	165×229	6.5×9	153	34,400

1.2.3 Bearing Defects in Railway Systems

As the roller bearing rotates, cyclic hertzian contact stress between the rollers and raceways are applied causing rolling contact fatigue (RCF). Roller bearings often propagate defects on the subcomponents exposed to rolling contact fatigue, being the cones, cups, and rollers. The damage caused by the contact fatigue increases substantially when subsurface inclusions (i.e., impurities in the metal used to manufacture the bearing) exist in regions of elevated subsurface shear stress. Micro-fissures may initiate at these impurities and over the course of many operating cycles, may propagate to the surface and result in small pits. These small pits lead to spalling as the material breaks away from the surface occurring on the raceways of the bearings and rollers, as shown in Figure 2. Lubricant contamination is another cause of bearing failure. Lubricant contamination occurs when defective seals allow contaminants, such as dirt or water, to enter the lubrication grease, resulting in the degradation of its performance. Contamination corrodes the surfaces of the raceways, leading to water-etched distributed defects, such as the one pictured in Figure 3.

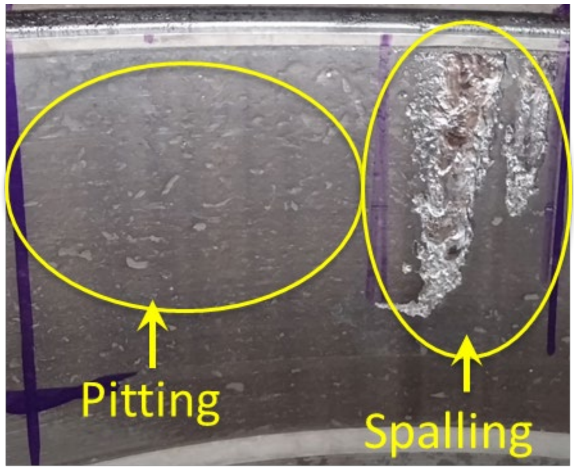

Figure 2: Localized bearing defects (pitting and spalling).

Figure 3: Water-etched bearing defect.

1.3 Current Maintenance Systems

Standard industry monitoring practices rely heavily on wayside inspection technologies. These technologies focus on three metrics: temperature, acoustics, and load. Wayside detectors provide intermittent snapshots of equipment health as a train passes their fixed trackside locations.

1.3.1 Hot Bearing Detectors (HBDs)

Hot bearing detectors (HBDs) are among the most widely implemented condition-monitoring systems in the railroad industry. These detectors are installed trackside at fixed intervals, typically every 25 to 40 km (~15 to 25 mi), to measure the bearing cup (outer ring) surface temperature as a train passes. Infrared sensors within HBDs measure the thermal profile of bearings in service and trigger an alarm if the measured temperature exceeds 94.4°C (170°F) above ambient [1]. Figure 4 shows a schematic diagram of an HBD.

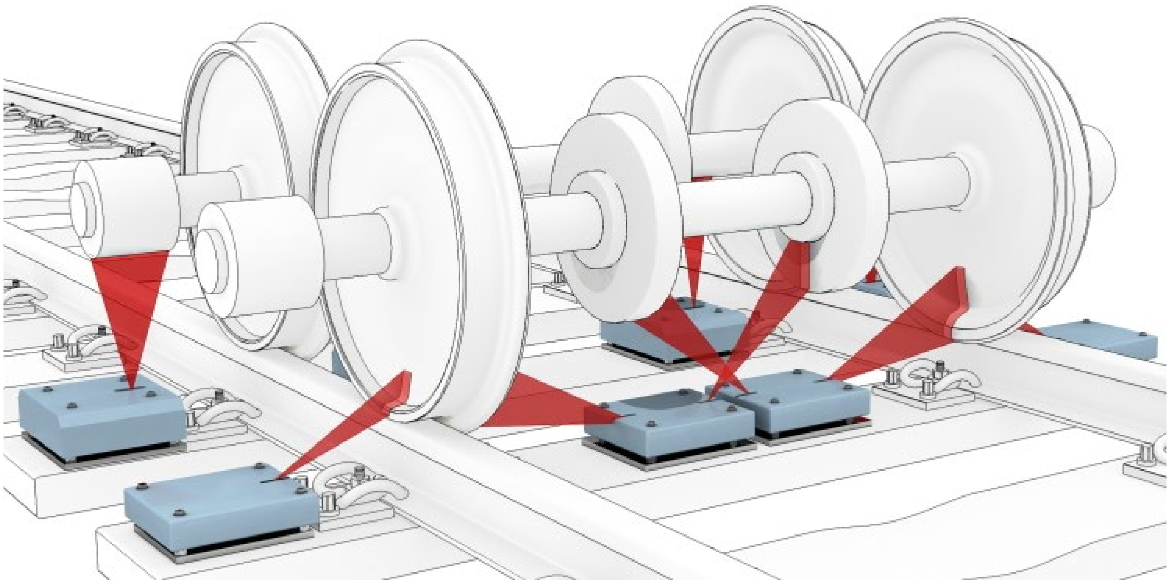

Figure 4: Hot Bearing Detector (HBD) diagram [7].

HBDs provide a simple and non-intrusive method for identifying severely deteriorated railway bearings; however, their effectiveness is limited by several fundamental issues. The first challenge is using temperature as the primary indicator of bearing deterioration. The drawback of relying on temperature is that it is a highly reactive indicator; by the time an over-temperature condition is detected, the bearing defect is often already in an advanced stage and may be beyond intervention. Additionally, it falls short in detecting early-stage spalling, pitting, or lubrication degradation that do not immediately manifest as a significant temperature increase. As a result, a bearing may progress through a large portion of its failure cycle while remaining below the AAR suggested HBD temperature alarm threshold, only truly activating when a bearing is nearing its end of operational life cycle. Secondly, the fixed-location nature of HBD systems is another shortcoming of these trackside detection systems. In North America, there are approximately

6,000 HBDs in service [1]. Given that measurements are only taken as a train passes a detection site, the monitored condition of a bearing is dependent on detector spacing rather than by changes to condition. The time intervals between detectors may be significant enough as to where defects may deteriorate undetected. Failing bearings between wayside stations pose a considerable safety risk, especially under high-load, high-speed, or extreme-weather conditions, where degradation can accelerate rapidly. If a late-stage defect is detected and the train requires immediate inspection, the time it takes to stop may be insufficient to prevent a catastrophic failure [7].

1.3.2 Acoustic Bearing Detectors (ABDs) and Track Acoustic Detector Systems (TADS™)

The second most common wayside condition monitoring systems are Acoustic Bearing Detectors (ABDs) and Track Acoustic Detector Systems (TADS™), which use microphones and accelerometers mounted near the rails to capture acoustic emissions of tapered roller bearings. An example of a TADS™ wayside monitoring system is shown in Figure 5. Severely spalled bearings identified by TADS™ are referred to as “growlers”. A detected “growler” will signal an immediate train stoppage to begin the inspection of the defective component.

Figure 5: Track Acoustic Detector System (TADS™) at rail side [1].

1.3.3 Wheel Impact Load Detectors (WILDs)

Wheel Impact Load Detectors (WILDs), as the one pictured in Figure 6, are another wayside condition monitoring method that use strain gauges to measure the vertical impact forces on train wheelsets and bearing assemblies. This measure is taken to prevent excessive wheel-rail impacts that can lead to catastrophic failure. Like HBDs, ABDs, and TADS™, WILDs are scarce and hence provide intermittent monitoring of the millions of wheels in operation on the North American rail system, which limits their effectiveness.

Figure 6: Wheel Impact Load Detectors (WILD) field installation.

1.4 Onboard Wireless Condition Monitoring Systems

Onboard wireless condition monitoring systems represent a modern shift from periodic wayside inspection to continuous, real-time health assessment of railway bearings and wheels. These onboard sensors are integrated with accelerometers, thermocouples, strain gauges, and are equipped with low-power wireless transmitters that relay data to a central receiver or cloud-based platform. Additionally, these sensors enable live monitoring of bearing and wheel health metrics, such as vibration, temperature, and load, to support proactive maintenance. Their continuous data stream supports advanced diagnostics, machine-learning-based predictions, and provides insight into trend analysis. Despite their advantages over trackside condition monitoring methods, challenges such as battery life, data bandwidth limitations, and environmental durability remain active areas of development for onboard wireless technologies within the industry.

1.4.1 UTCRS Wireless Sensor System

The University Transportation Center for Railway Safety (UTCRS) research team designed, validated, and licensed a wireless sensor that can accurately and reliably monitor the condition of freight rail bearings and wheels via vibration and temperature signatures in a non-intrusive manner. A picture of the prototype wireless sensor that has been licensed to Hum Industrial Technology, Inc., is shown in Figure 7. The wired version of this same sensor that is also mounted on the adapter is used as a reference to compare against and validate the accuracy of the wireless sensor. Note that, in field deployment, only the wireless sensor module that Hum developed is mounted on the bearing adapter.

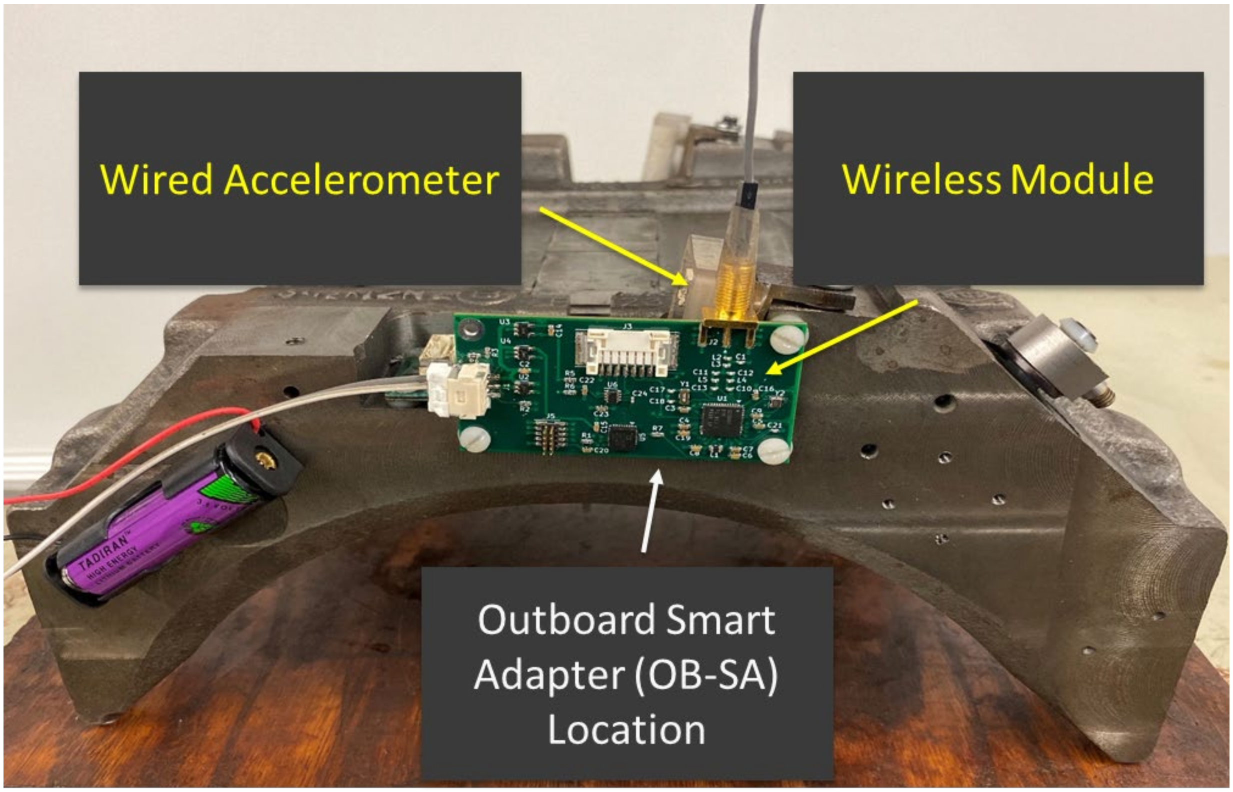

Figure 7: UTCRS wireless onboard sensor [8].

The Hum licensed version of the UTCRS onboard sensor mounts on the bearing adapter, enabling reuse of the same sensor after a wheelset has been pulled from service. The laboratory version of this wireless sensor collects data at a sampling rate of 5.12 kHz for 16 seconds every 10 minutes. This data is then sent to a central monitoring unit via Bluetooth [8].

1.5 Related Work

In August 2024, the UTCRS published a thesis by Kevin Quaye titled "Feature Extraction from Vibration Signature Acquired from Railroad Bearing Onboard Condition Monitoring Sensor Modules" [9]. In his work, Kevin Quaye summarized the implementation and performance of three machine learning regression models that used vibration data collected by the UTCRS to predict bearing speed, which is a key feature used in the health assessment and analysis of railroad bearings. Traditional references, such as Global Positioning System (GPS), are impractical within the current framework of onboard systems due to power constraints, asynchrony with onboard data, and signal interference. This motivated Quaye's exploration of a data-driven approach capable of inferring speed directly from vibration signatures.

Quaye evaluated three regression algorithms: Random Forest, XGBoost, and Linear Regression. From his data, he derived three primary input features: (1) the power spectral density (PSD) of the signal, (2) the corresponding frequencies, and (3) the load condition of the bearing (unloaded or fully loaded). His results showed that the PSD carries enough information to estimate the rotational speed under laboratory conditions, with his best performing model achieving a coefficient of determination (R^2) greater than 0.8. The coefficient of determination is a statistical measure that indicates how well a prediction fits the data. These findings validated the feasibility of extracting speed from vibration data without relying on external instrumentation, thereby enhancing the potential autonomy of onboard condition-monitoring systems.

Quaye's study laid the foundation for subsequent research by demonstrating that vibration-based speed estimation is practical and has the potential to be integrated directly into onboard systems. However, his work demonstrated an important limitation: the vibration datasets used in his study were not signal processed prior to feature extraction. Raw vibration signals from defective bearings are often dominated by broadband noise, impacts, and transient events, which can obscure defect-related characteristics. Without the application of signal processing techniques, machine-learning models may learn patterns driven by noise rather than true mechanical behavior.

In contrast, this study incorporates advanced signal-processing techniques, including envelope extraction, harmonic matching, signal filtering (lowpass, bandpass, and wavelet), and pairwise spacing analysis, to strengthen defect-related harmonic structure prior to speed estimation. These methods are especially critical at high speeds and low loads, where vibration amplitudes are easily masked by noise. By integrating robust signal processing with machine learning, this work provides a more reliable framework for estimating speed from vibration signatures.

1.6 Motivation

A driving force motivating the research at the UTCRS is the proactive monitoring of railway bearings. To this end, several algorithms have been developed by researchers at the UTCRS to analyze and diagnose bearing conditions. Figure 8 shows an overall flowchart of the optimized defect algorithm developed by Amy Gonzalez and Joseph Montalvo [6] [10]. Level 2 of this defect detection algorithm notably uses speed as a key input to determine the defective component in a bearing.

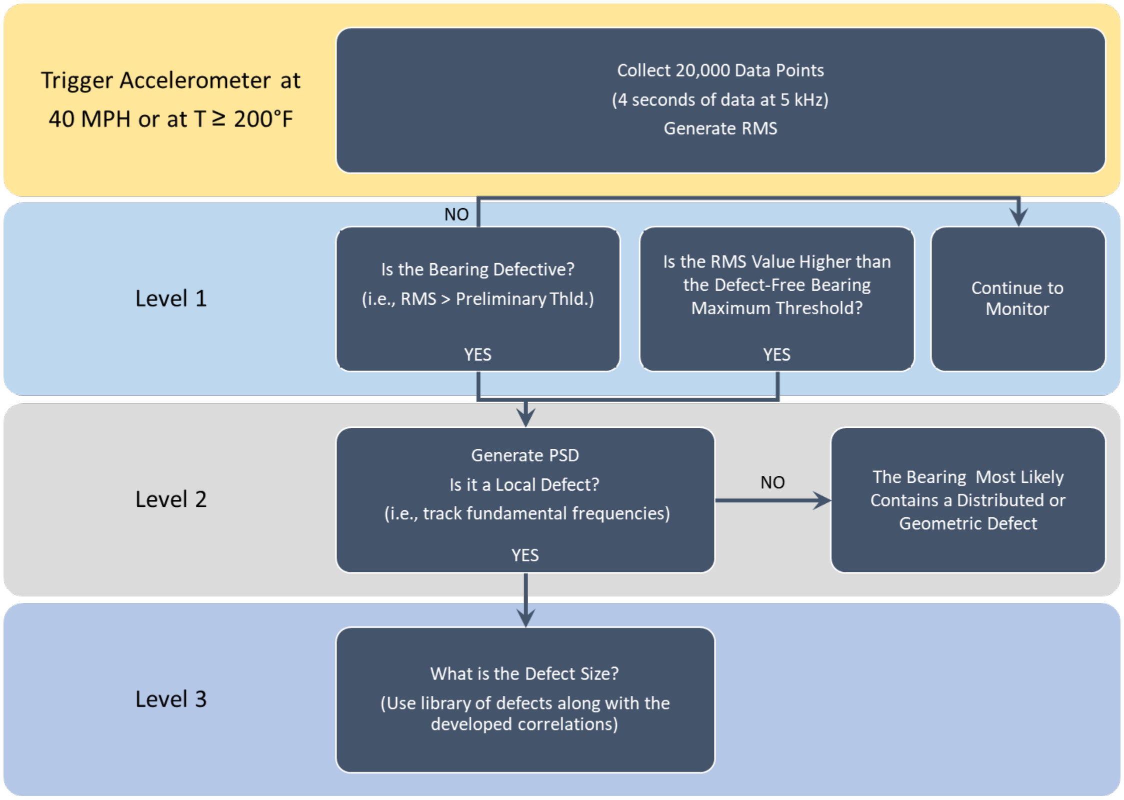

Figure 8: Flowchart of the optimized railroad bearing defect-detection algorithm [10].

The optimized defect detection algorithm determines the presence of a defect in a bearing, identifies the defective component, and estimates the defect area. These are broken down into three levels. Level 1 analysis assesses bearing health by checking for the presence of a defect using the root mean square (RMS) of the vibration data and comparing it to a set of preliminary safety thresholds, refined most recently by Jeffery Pams in 2024 [11].

Level 2 analysis uses the fundamental frequencies and a generated power spectral density (PSD) of the vibration signatures to compare the defect energies of the three bearing components subjected to rolling contact fatigue. To reiterate, the three components analyzed are the cup (outer raceway), cone (inner raceway), and rollers. The algorithm calculates the fundamental frequencies and their harmonics given the rotational speed of tapered roller bearings to analyze the energies of each defective component. Using these defect energies, a confidence score is created to denote which component is defective within the tapered roller bearing.

The fundamental frequency equations are based on work done by Tarawneh *et al*, [12]. The six fundamental frequency equations are listed as Equations (1)-(6).

$$\omega_{cone} = \omega_o \tag{1}$$

$$\omega_{cage} = \left(\frac{R_{cone}}{R_{cone} + R_{cup}}\right)\omega_{cone} \tag{2}$$

$$\omega_{roller} = \left(\frac{R_{cone}}{D_{roller}}\right)\omega_{cone} \tag{3}$$

$$\omega_{out} = 23\omega_{cage} \tag{4}$$

$$\omega_{in} = 23(\,\omega_{cone} - \omega_{cage}) \tag{5}$$

$$\omega_{rolldef} = \left(\frac{R_{cup}}{R_{roller}}\right)\omega_{cage} \tag{6}$$

ω_{cone} and ω_o represent the bearing rotational speed in Hz. R_{cone}, R_{cup}, and R_{roller} represent the radii of the cone (inner raceway), cup (outer raceway), and roller, respectively. D_{roller} is the diameter of the roller. The equations are split between three fundamental frequencies (Equations (1)-(3)) and three defect frequencies (Equations (4)-(6)). Level 3 analysis outputs a prediction for the defect size by using empirically developed relationships between the RMS of the acceleration and the corresponding defect areas [6].

The work featured in this manuscript aims to directly contribute to the autonomy of the level 2 analysis framework. The level 2 defect-energy analysis relies on knowing the bearing rotational speed; however, this information is not always available from the current framework of onboard systems. The train speed is often obtained from GPS-based measurements, which do not provide instantaneous data, can be power-intensive, and are susceptible to signal interference.

This work enables the usage of level 2 analysis on field deployed onboard sensors by developing a vibration-based machine learning model capable of extracting the instantaneous rotational speed from acquired vibration signatures and using it to identify the damaged component within the bearing.

CHAPTER II

MACHINE LEARNING MODELS AND RELEVANT STUDIES

2.1 Machine Learning Background

Machine Learning (ML) is a popular subfield of Artificial Intelligence (AI) that enables algorithms to automatically learn patterns and relationships from large datasets. By training on extensive datasets, ML models can classify behaviors and make predictions that would otherwise be difficult to achieve using traditional methods. Moreover, ML offers an adaptive framework for modeling system behavior, supports anomaly detection, and enables analysis of high-dimensional data.

2.1.1 Supervised Learning

Supervised learning is a category within machine learning that involves training an algorithm using input-output pairs, where each data sample x_i is associated with a known output y_i. Typically, in supervised learning, the objective for the model is to learn the relationship between the input features and output values, such that the algorithm can predict outputs for unseen data after training. In the context of railway bearing speed estimation, Kevin Quaye, a researcher for the UTCRS, implemented a supervised learning approach using regression models to predict bearing speed [9]. The availability of the ground-truth speed allowed the model to learn the direct relationship between the input features and the operational speed.

2.1.2 Unsupervised Learning

In contrast to supervised learning, unsupervised learning operates on datasets without labeled outputs, seeking to uncover hidden patterns or groupings within the data. Since there are no ground truths to relate to the input features, the models must infer relationships based on the characteristics of the dataset. Clustering, a method deployed in this study, is one of the most popular forms of unsupervised learning that groups data based on similarities or differences in behavior.

2.1.3 K-Means Clustering

K-Means clustering is a machine learning algorithm that uses an unsupervised approach, partitioning data into *k* distinct groups based on proximity. K-Means works iteratively, assigning each data point to the nearest centroid (the center of a cluster), then recalculating these centroids as the mean of the newly clustered data points. This is demonstrated visually in Figure 9, where data points are color-coded and grouped by their centroids. This iterative process is done until assignments stabilize.

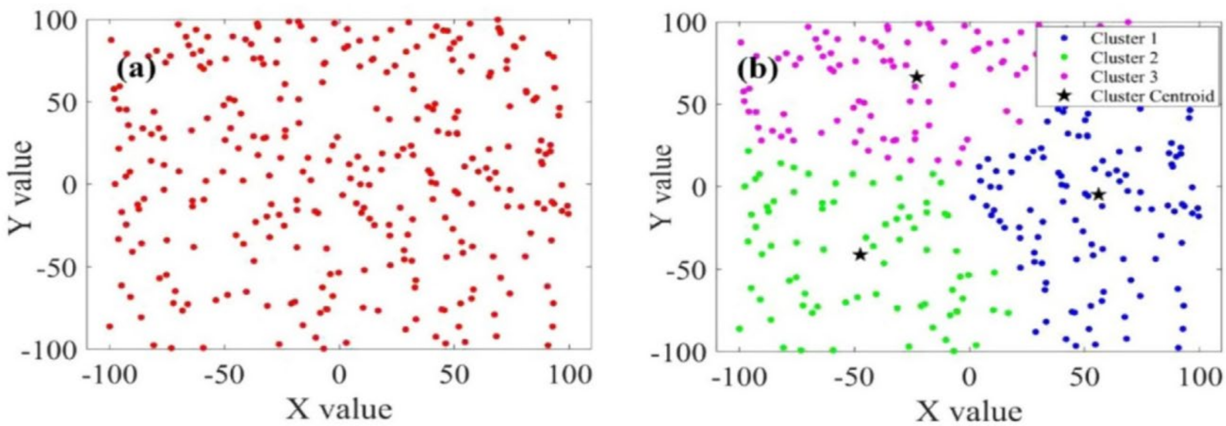

Figure 9: K-Means Clustering [13].

Stabilization of the assignment indicates that a minimum error threshold has been reached. K-Means is especially effective at identifying relationships by using the distance between data points, essentially identifying natural groupings in datasets where structures may not be explicitly labeled. Mathematically, the objective function of the K-Means algorithm seeks to minimize the within-cluster sum of squared distances (WCSS) as shown in Equation (7) [13].

$$J = \sum_{i=1}^{k} \sum_{x_j \in C_i} \left|\left|x_j - \mu_i\right|\right|^2 \tag{7}$$

Here x_j represents the current data point, C_i is the set of points assigned to a cluster i, μ_i is the centroid (mean) of cluster i, and $\left|\left|x_j - \mu_i\right|\right|^2$ represents the squared Euclidean distance between point x_j and its centroid. Equation (8) describes how the data points are assigned to a cluster.

$$C_i = \left\{x_j : \left|\left|x_j - \mu_i\right|\right|^2 \leq \left|\left|x_j - \mu_l\right|\right|^2, \forall l \in \{1, \dots, k\}\right\} \tag{8}$$

Here the l subscript denotes the previous cluster. Each centroid is then recalculated as the mean of all the points assigned to that cluster, as shown in Equation (9).

$$\mu_i = \frac{1}{|C_i|} \sum_{x_j \in C_i} x_j \tag{9}$$

These steps are repeated until the change in centroids fall below a pre-defined threshold or the error stabilizes. In this study, K-Means is used to estimate the true harmonic spacing and yields the fundamental defect frequency by identifying the most dominant cluster centroid. The use of K-Means allows the algorithm to distinguish noise, account for spurious peaks, and handle missing harmonics that may occur in extreme speed conditions. The fundamental defect frequency is then used to reverse calculate the rotational speed of the bearing.

2.2 Algorithm Performance and Scoring Systems

The performance and robustness of the speed-extraction algorithm presented in this study requires a structured scoring system capable of assessing both the prediction accuracy and the quality of harmonic behavior extracted from the vibration spectrum. It is important to evaluate more than just predicted speed due to noisy vibration signals, especially when defects are present. The scoring systems presented in this study are absolute error, relative error, and a composite score with harmonic alignment.

2.2.1 Error Scoring Methodology

The evaluation in this study focuses on both individual and aggregate cases, measured using absolute error, relative error, and harmonic error. Evaluation of individual cases refers to performance assessed within a specific speed range under a single loading condition with a specified defect type. Aggregate evaluation considers the performance across both unloaded and loaded conditions within the same speed range and overall speed settings. The importance of individual case evaluation is due to the variation in vibration responses caused by unique combinations of load, speed, and defect type. These conditions produce unique signatures, indicating that the characteristics of one case cannot be generalized to another. The absolute error, depicted in Equation (10), quantifies the direct difference between the estimated rotational speed and the reference speed.

$$E_{abs} = \left|\hat{S} - S_{true}\right| \tag{10}$$

E_{abs} represents the absolute error, $\hat{S}$ represents the estimated bearing speed in rotations per minute (RPM), and S_{true} is the reference speed of the bearing. The relative error (Equation (11)) is a ratio between the absolute error and the actual speed, providing a dimensionless metric that is independent of operating speed.

$$E_{rel} = \frac{\left|\hat{S} - S_{true}\right|}{S_{true}} \tag{11}$$

Bearing defect frequencies manifest in multiple harmonics, therefore the algorithm is designed to evaluate the alignment between the detected and true harmonics. As mentioned previously, the harmonics of bearing defects may deviate due to the shifting of mechanical components. This shifting of frequencies is the result of slippage or skidding of rollers within the bearing cone assembly or due to variations in geometric tolerances of bearing components. A hunting range is therefore applied to find the true harmonic from the current value to accommodate for this shifting [10]. Harmonic error is applied to the scoring metrics to quantify the effects of this hunting. If a fundamental defect frequency (f_{true}) is found, the expected harmonics are shown in Equation (12).

$$H_{expected} = kf_{true}, \quad k = 1, 2, \dots, N \tag{12}$$

For each harmonic, the deviation between the detected peak and its expected location is computed as shown in Equation (13).

$$E_{harm} = \frac{1}{N} \sum_{k=1}^{N} \frac{|f_{k,det} - kf_{true}|}{kf_{true}} \tag{13}$$

Minimizing the harmonic error ensures that the fundamental spacing is captured through the consistency of the harmonics rather than the amplitude of the fundamental defect frequency, which is especially important in low operating conditions where the fundamental defect frequencies are lower.

The aggregate evaluation of algorithm performance is computed by taking the mean absolute error (MAE) and the mean relative error (MRE), represented in Equations (14) and (15). Computation for the MAE and MRE is done for an overall dataset and includes all types of load, speed, and defect combinations. To retrieve a more detailed performance overview, the MAE and MRE were also computed on individual cases that represented a specific combination of speed, load, and defect type.

$$MAE = \frac{1}{n} \sum_{i=1}^{n} \left| \hat{S} - S_{true} \right| \tag{14}$$

$$MRE = \frac{1}{n}\sum_{i=1}^{n}\frac{|\hat{S} - S_{true}|}{S_{true}} \tag{15}$$

In these equations, S_{true} represents the actual reference speed, $\hat{S}$ is the output rotational speed, and n represents the number of instances.

2.3 Confidence Score Methods

Two confidence scoring methods were utilized in this study. Initially, the speed extraction algorithm generated an internally defined confidence score based on the RMS vibration levels, harmonic alignment, and consensus scoring across six different filter-envelope combinations. These filter-envelope combinations were discussed earlier in CHAPTER I. This confidence score was used to compare candidate combinations. However, this confidence scoring method, however, did not directly leverage the established defect energy framework used by the UTCRS. For more direct integration, a second confidence scoring system that uses the speed estimation as an input into the defect-detection algorithm developed by Montalvo [6] and Gonzalez [10] was established. The first confidence scoring method was utilized for a K-Means clustering based speed approximation while the second confidence scoring method was used as the primary indicator for future field implementation.

2.3.1 RMS-Based Consensus Scoring Method

The first confidence scoring method utilized the acceleration data and a consensus score to gauge performance. The algorithm favored a certain speed prediction when several of the six filter-envelope combinations output similar defect frequencies. For each filter-envelope combination, the algorithm used the error metrics mentioned in Section 2.2.1. A speed-dependent RMS threshold was calculated as seen in Equation (16), using the predicted speed output by the feature extraction algorithm. This calculated threshold was compared to the established UTCRS thresholds updated most recently by Jeffery Pams [11]. The estimated RMS threshold is compared to the true calculated RMS of the vibration profile (RMS_{true}) captured by the micro-electro-mechanical system (MEMS)-based accelerometers.

$$RMS_{thresh,est} = 0.0113 \cdot RPM_{est} - 0.839 \tag{16}$$

A ratio is obtained formed between the measured RMS and an RMS value approximated from the calculated threshold as seen in Equation (17). This ratio is then mapped through a logistic function to obtain a scalar confidence score, as shown in Equation (18). The small shape parameter s is set to 0.1. It should be noted that the output confidence scores (*Confscore*) were probability clipped to avoid binary outputs (0 or 1) that would skew the model. More specifically, a range between 5% and 95% was selected to avoid outputting extreme confidence scores of 0% or 100%.

$$ratio = \frac{RMS_{true}}{RMS_{thresh,est}} \tag{17}$$

$$Confscore = \frac{1}{1 + \exp\left(-\frac{ratio - 1}{s}\right)} \tag{18}$$

The estimated RMS threshold was programmed to penalize predictions greater than 8.16 GRMS as this value correlates to the established maximum threshold at the highest testing speed of 796 rpm (85 mph). Additionally, a frequency-based consensus score was formulated by comparing each predicted defect frequency to the modal value across the six filter-envelope combinations. The final original confidence metric was defined as the maximum of the signal confidence and the consensus-based term seen in Equation (19). This included the penalties when the estimated RMS thresholds exceeded 8.16 GRMS.

$$FinalConfidence = \max\left(Confscore, exp\left(-\frac{\left|\hat{f}_{det} - f_{mode}\right|}{\alpha}\right) - \delta_{rms}\right) \tag{19}$$

In Equation (19), $\hat{f}_{det}$ represents the individually output detected defect frequencies, f_{mode} is the mode of all six individual outputs, α is the consensus decay scale equal to 1, and the δ_{rms} represents the RMS penalty applied.

2.3.2 Defect Energy Based Confidence Scoring Method

To obtain a confidence score more directly associated with the periodic nature of a bearing defect, a second scoring strategy was devised using the defect-detection algorithm developed by Montalvo and Gonzalez [6] [10]. The output speeds were fed into the defect detection algorithm for each time instance, or instantaneous shot of data. The algorithm then computed the PSD and located the local PSD maxima around the theoretical frequencies to determine the actual defect frequencies. These peaks were then integrated to determine the PSD energies within narrow bands centered around harmonics that are based on the predicted speeds from the six filter-envelope combinations. The resulting defect energies were squared and normalized across defect types that are finally converted into percent values for each accelerometer channel.

CHAPTER III

FEATURE EXTRACTION ALGORITHM

3.1 Feature Extraction Framework

A robust feature extraction framework was developed to estimate rotational speed and underlying bearing defects. This framework, described schematically in Figure 10, uses multiple signal processing techniques in conjunction with a K-Means machine learning algorithm designed to isolate the dominant patterns in the vibration signal associated with bearing faults under varying operating conditions.

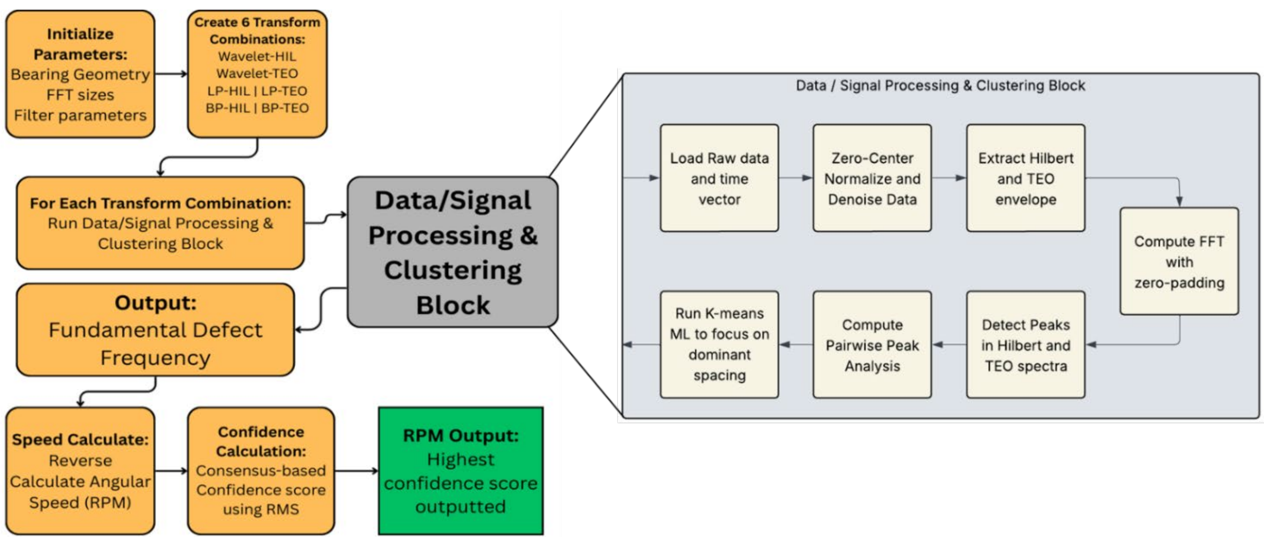

Figure 10: Feature Extraction Methodology Framework.

The most notable aspect in this framework is the “Data/ Signal Processing & Clustering Block”. In this section, the process begins by computing a zero-center normalization of the raw accelerometer data in the time domain, followed by filtering techniques to denoise the data. The algorithm leverages the behavior of six filter-envelope combinations to determine the rotational speed in various operating conditions by using three filter types and two envelope extraction techniques. The three filter techniques used are wavelet, lowpass, and bandpass filters. Two envelope extractions, the Hilbert envelope (HIL) and the Teager energy operator (TEO), were performed on each of these filters. Hence, six filter-envelope combinations were considered: Wavelet-HIL, Wavelet-TEO, Lowpass-HIL, Lowpass-TEO, Bandpass-HIL, and Bandpass-TEO. Each of these algorithms individually output a distinct transformed vibration signal in the frequency domain, allowing for the determination of dominant signals and the computation of pairwise peak analyses. The K-Means ML algorithm is then implemented to obtain the fundamental defect frequency.

3.1.1 Data and Signal Processing

The data and signal processing stage forms the basis of the feature extraction framework and creates a distinct approach in locating the defect frequency by enhancing the visibility of defect-related harmonic content within the vibration signal. Raw accelerometer data captured from tapered roller bearings, like that shown in Figure 11, contain broadband noise, transient impacts, and structural resonance effects that obscure the periodic signals that aid in accurately predicting speed.

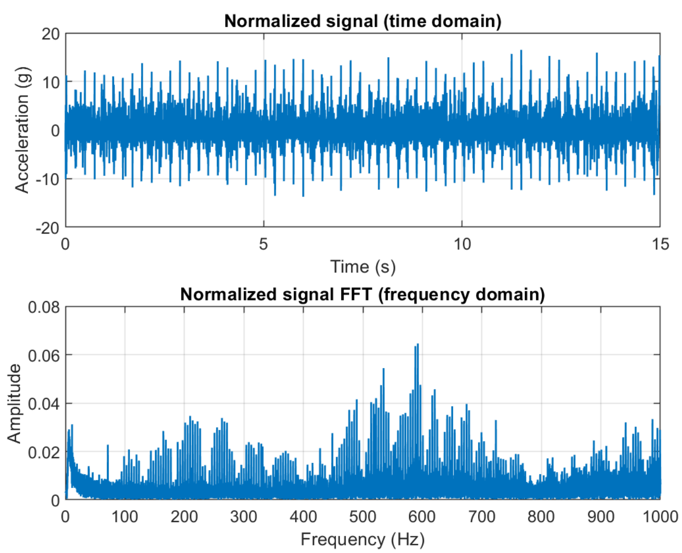

Figure 11: Normalized raw vibration signal in time and frequency domains.

3.1.2 Denoising Techniques

Lowpass filtering smoothens a signal by removing values above a specified cutoff frequency. More specifically, an infinite impulse response (IIR) lowpass filter is applied to retain the lower-frequency dynamics where the target bearing harmonics occur. The IIR lowpass filter is implemented due to its computational efficiency and its ability to achieve sharp cutoff characteristics. Additionally, it is often seen that signals after 1 kHz become extremely populated by noise and are not helpful for speed prediction. The cutoff frequency was set to 700 Hz, which retained enough harmonics to accurately detect the defect frequencies. Testing demonstrated that setting the lowpass cutoff at a frequency higher than 700 Hz introduced noise that skewed the results of the algorithm. Figure 12 shows the applied lowpass filter.

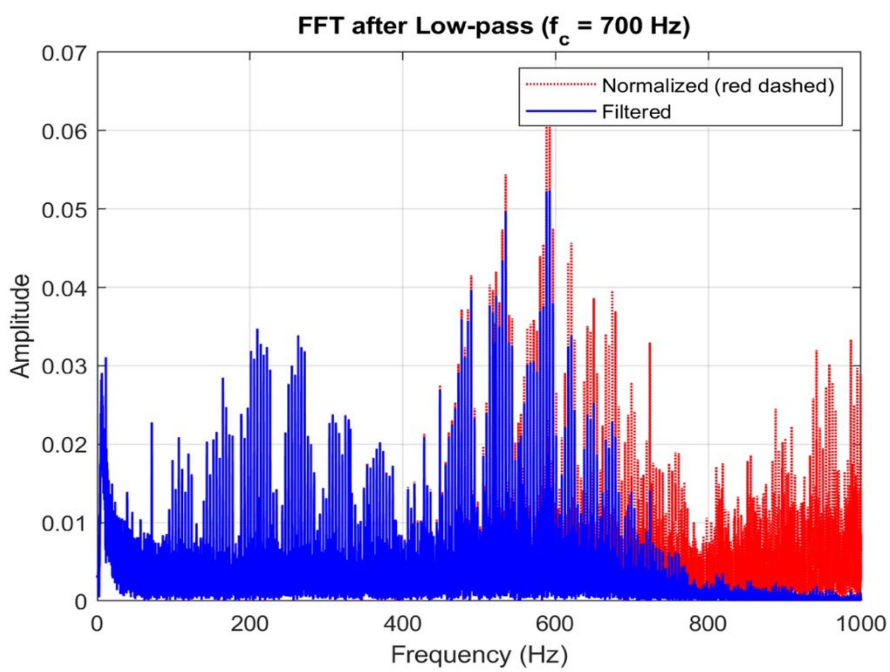

Figure 12: Normalized and low-pass filtered signal of a cone-defective bearing at 234 rpm and 17% load.

Bandpass filtering isolates a targeted frequency band where expected defect-related harmonics are expected to appear, while attenuating frequencies outside of the specified frequency band. In this case, a bandpass range of 35-420 Hz was selected after sensitivity analysis was conducted. The low-frequency cutoff was initially set to 40 Hz in order to capture the fundamental defect frequencies associated with the lowest operating speed. However, the low-frequency cutoff was changed to 35 Hz when accounting for possible defect frequency shifting. The 420 Hz was selected to retain several harmonics, while attenuating possible noise introduced at higher frequencies. Figure 13 compares a normalized and a bandpass-filtered signal.

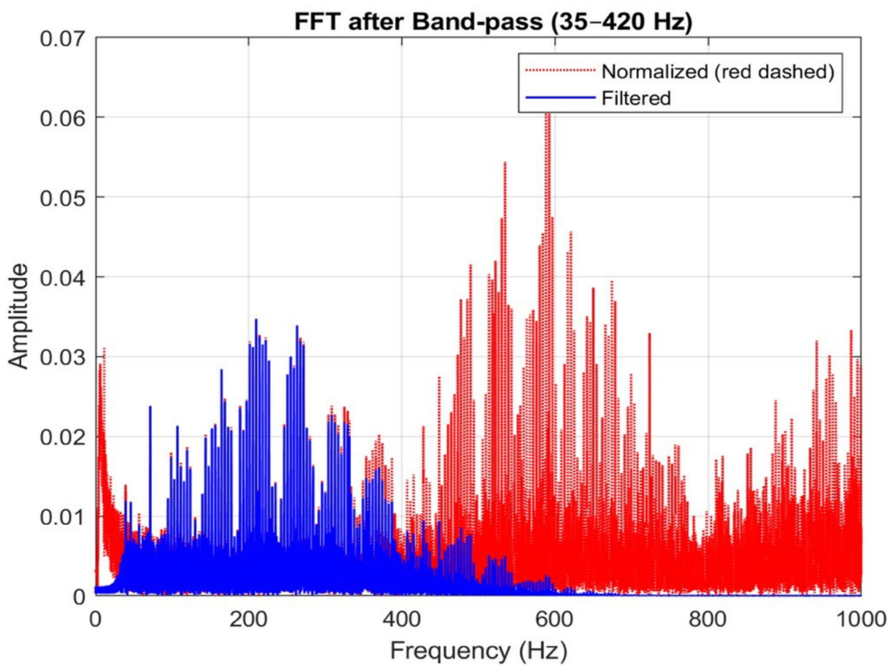

Figure 13: Normalized and bandpass-filtered signal of a cone-defective bearing at 234 rpm and 17% load.

Wavelet-based denoising offers a more adaptive method for noise suppression compared to traditional filtering methods. The wavelet denoising decomposes the vibration signal into multiple time-frequency coefficients using a discrete wavelet transform (DWT) rather than solely using signals in the frequency domain. Larger time-frequency coefficients are representative of noise-free signals, while small magnitude coefficients represent noise. Equation (20) represents the DWT,

$$x(t) = \sum_k c_{J,k}\phi_{J,k}(t) + \sum_{j=1}^{J}\sum_k d_{j,k}\psi_{j,k}(t) \tag{20}$$

where $\phi_{J,k}(t)$ is the scaling function, $\psi_{j,k}(t)$ is the wavelet function, $c_{J,k}$ represents the approximation coefficients at level J, and $d_{j,k}$ are the detail coefficients at level j. The scaling function $\phi_{J,k}(t)$ represents "coarse", or low-frequency, structure of the signal. The scaling functions, shown in Equation (21), capture slow-varying components and provide a large-scale framework of the multiresolution analysis. The scaling function exhibits lowpass filter behavior, outputting a higher cutoff. In contrast, the wavelet function $\psi_{J,k}(t)$ exhibits highpass behavior, and is defined using the scaling function given by Equation (22),

$$\phi(t) = \sum_n h[n]\phi(2t-n) \tag{21}$$

$$\psi_{J,k}(t) = \sum_n g[n]\phi(2t-n) \tag{22}$$

where $h[n]$ and $g[n]$ are the lowpass and highpass coefficients, respectively. These two-scale relations show that both functions are constructed through a dyadic scaling and shifting of $\phi(t)$. This process links the DWT to a pair of mirror filters that essentially represent a lowpass and highpass filter. The detail coefficients that represent noise are then eliminated by applying a soft thresholding described by Equation (23).

$$\widetilde{d_{J,k}} = \begin{cases} sign(d_{j,k})(|d_{j,k}| - \lambda_j), & |d_{j,k}| > \lambda_j \\ 0, & |d_{j,k}| \leq \lambda_j \end{cases} \tag{23}$$

In Equation (23), λ_j is the threshold for level j, $d_{j,k}$ is the original detail coefficients, and $\widetilde{d_{J,k}}$ are the thresholded coefficients after eliminating noise-representative coefficients. The inverse DWT reconstructs the signal, preserving the essential periodic features of the original signal while reducing noise. The wavelet filtered signal can be visualized in Figure 14.

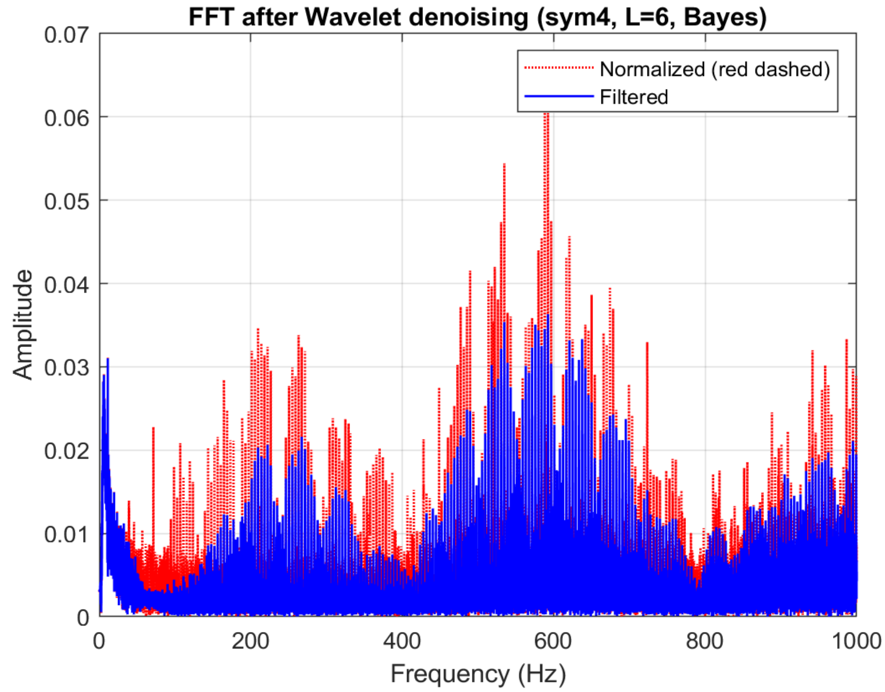

Figure 14: Normalized and wavelet-filtered signal for a cone-defective bearing at 234 rpm and 17% load.

3.1.3 Envelope Extraction

The envelope extractions serves to demodulate the vibration signal and reveal modulations caused by repeated impacts. Defect-related impacts create impulse events that modulate underlying rotational frequencies. The Hilbert (HIL) envelope is a widely used technique for demodulating signals in rotating machinery analysis, and the Teager energy operator (TEO), also known as Teager-Kaiser energy operator (TKEO), allows for a nonlinear approach to extract amplitude modulations of a vibration signal. Representative signals of both envelope extractions in the time domain for a bearing with a cone defect running at 234 rpm and 17% load are displayed in Figure 15.

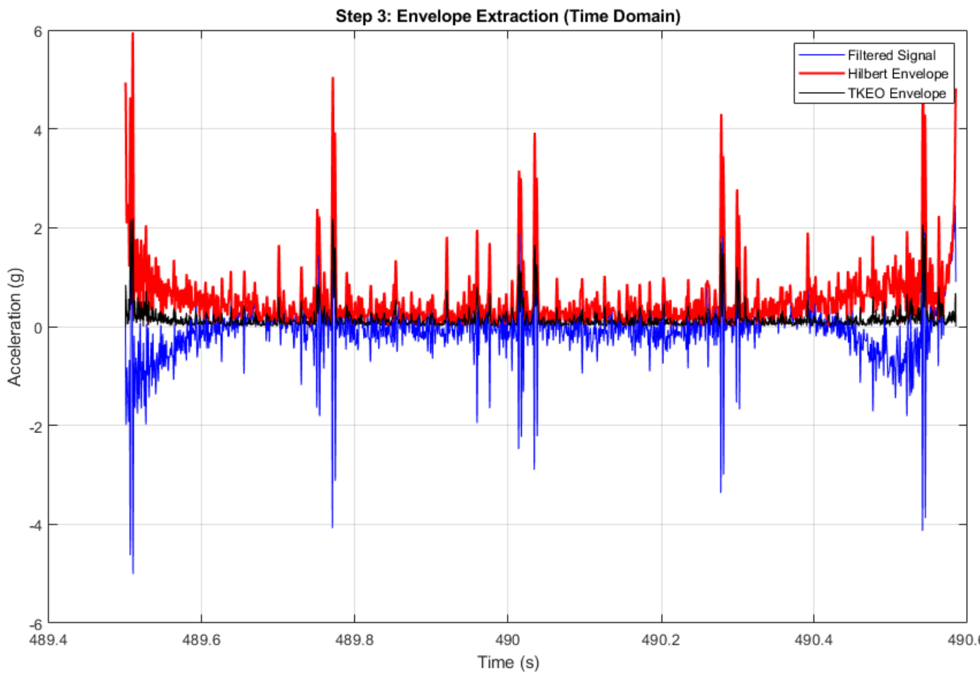

Figure 15: Envelope extraction comparison to filtered time-domain signal.

Hilbert (HIL) Envelope. The HIL transform provides a mathematical method to construct the analytical signal from which the envelope is derived. Given the filtered vibration signal $x(t)$, the Hilbert transform $\hat{x}(t)$ is given in Equation (24).

$$\hat{x}(t) = \mathrm{H}\{x(t)\} = \frac{1}{\pi}\mathrm{P.V.}\int_{-\infty}^{\infty}\frac{x(\tau)}{t-\tau}d\tau \tag{24}$$

$\mathrm{H}\{x(t)\}$ denotes the Hilbert transform of the raw time domain signal, and P.V. represents the Cauchy principal value of the integral. The HIL envelope is obtained by taking the absolute value of the analytical signal $z(t)$, which is constructed by adding the HIL-transformed signal multiplied by the square root of -1, otherwise seen as j, to the original time domain signal represented by Equations (25) and (26). It should be noted that for this study, the HIL envelope is performed after denoising. The HIL envelope is compared to a bandpass-filtered signal in Figure 16.

$$z(t) = x(t) + j\hat{x}(t) \tag{25}$$

$$HIL_{env}(t) = |z(t)| \quad (26)$$

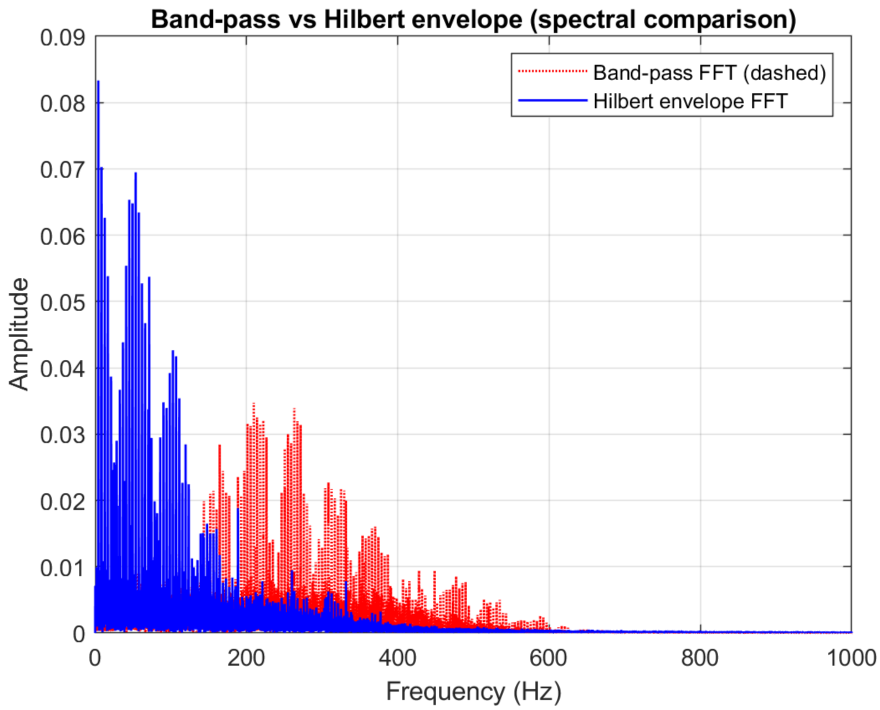

Figure 16: Hilbert envelope comparison to a filtered signal in the frequency domain.

Teager Energy Operator (TEO). The Teager energy operator (TEO) captures the instantaneous energy of the signal, making it highly sensitive to abrupt impact and transient features associated with bearing defects. The TEO is defined by Equation (27), and the TEO envelope is described as the square root of the absolute value of the TEO, as shown by Equation (28).

$$\mathrm{TEO} = \Psi\big[x[n]\big] = x^2[n] - x[n+1]\,x[n-1] \quad (27)$$

$$TEO_{env} = \sqrt{\big|\Psi\big[x[n]\big]\big|} \quad (28)$$

Where $x[n]$ represents a single datapoint found at $n = (1,2,\ldots,n)$. An envelope-like representation, emphasizing modulated components of the bearing vibration signal, is produced by applying the TEO to the time domain signal.

Both HIL and TEO envelopes are transformed into the frequency domain using a Fast Fourier Transform (FFT), producing a spectrum where the fundamental defect frequencies and their harmonics become more prominent. Figure 17 demonstrates the TEO envelope in the frequency domain compared to a bandpass-filtered signal with no envelope extraction. The algorithm outputs six individual filter-envelope combinations that will predict speed in various conditions. The rotational speed at various conditions is accurately predicted using these six combinations.

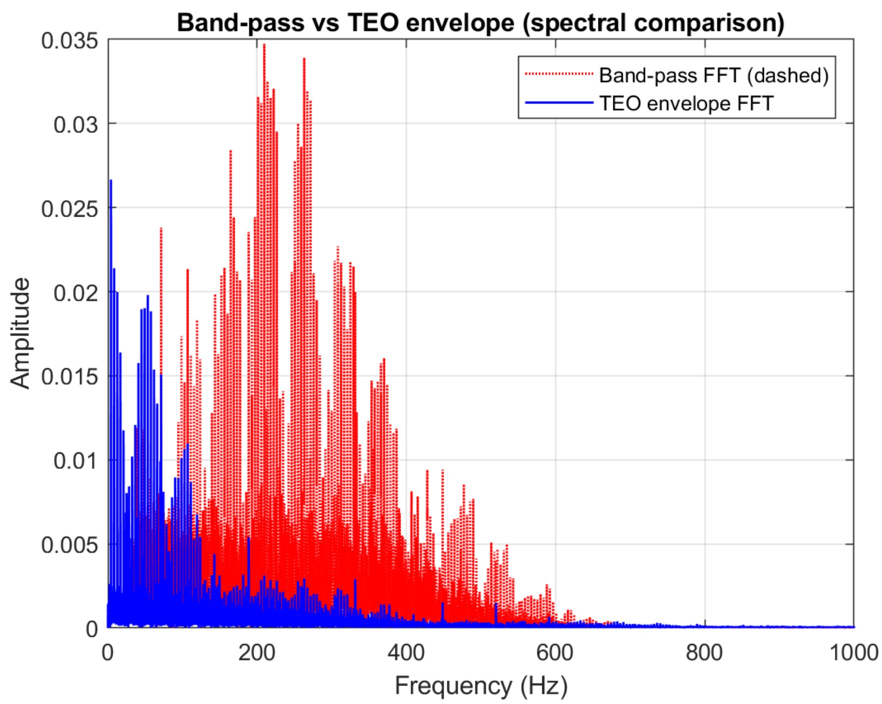

Figure 17: TEO envelope comparison to a bandpass-filtered signal in the frequency domain.

3.1.4 Speed Extraction

The final three stages within the “Data/ Signal Processing and Clustering” block in Figure 10 represent the fundamental defect frequency extraction. Identifying the spacing between the spectral peaks makes it possible to calculate the true rotational speed due to the correlation between the fundamental defect frequency and the rotational frequency (speed) of the bearing.

Speed extraction is achieved by pairwise peak analysis, K-Means clustering, and reverse calculation using the fundamental frequency Equations (1) through (6) [12]. Three parameters are established to compute the pairwise peak analysis: minimum peak height, minimum peak prominence, and minimum peak spacing. Local maxima that fall within these parameters are considered as peaks for the analysis. Peaks must have an amplitude of at least 3% of the maximum amplitude of the signal, ensuring that only peaks with significant energy contributions are considered. The minimum peak prominence, or the lowest distance between a local maxima and minimum of the considered region, is set to 1.8% of the maximum amplitude of the signal. Finally, a minimum peak spacing of 5 Hz is imposed to prevent the algorithm from incorrectly selecting closely-spaced noise. These parameters output a set of peaks, F, and their corresponding frequencies, f_i, as seen in Equation (29). Equation (30) ensures that the operation is not performed multiple times for the same peak.

$$F = \{f_1, f_2, \dots, f_m\} \tag{29}$$

$$\Delta f_{ij} = |f_i - f_j|, \quad i \neq j \tag{30}$$

Pairwise frequency spacings are computed between all possible combinations of peaks. The pairwise peak analysis generates a set of spacing values, shown in Equation (31), ready to be sent to the K-Means ML algorithm for clustering to find the dominant frequency spacings.

$$\Delta F = \{\Delta f_{12}, \Delta f_{13}, \dots, \Delta f_{ij}\} \tag{31}$$

The K-Means clustering algorithm is applied to the set of ΔF to identify the dominant spacing patterns corresponding to the true defect harmonics. The K-Means algorithm partitions spacing values into k clusters by using the objective function in Equation (7). The cluster with the smallest variance is assumed to represent the fundamental defect frequency or one of its early harmonics. Thus, Equation (32) shows that the extracted fundamental defect frequency is equal to the dominant centroid.

$$\hat{f}_{defect} = \mu_{dominant} \tag{32}$$

This study focuses primarily on the assumption that the known defect is located on either the cup or cone. Equation (33) represents the geometric constant for bearings with a cone defect, and Equation (34) represents geometric constants for bearings with a cup defect.

$$K_{in} = 23\left(1 - \frac{R_{cone}}{R_{cone} + R_{cup}}\right) \tag{33}$$

$$K_{out} = 23\left(\frac{R_{cone}}{R_{cone} + R_{cup}}\right) \tag{34}$$

These geometric constants are used to calculate the axle rotational frequency. The speed is calculated by dividing the estimated fundamental defect frequency by the corresponding geometric constant and multiplying by 60 to get the speed in rpm, as seen in Equation (35).

$$\hat{S} = 60 * \frac{\hat{f}_{defect}}{K_{in/out}} \tag{35}$$

Each filter-envelope combination outputs an individual predicted speed. These estimates are evaluated using the scoring methods mentioned in section 2.2.1. All individual speed predictions are input into the defect detection algorithm to determine a confidence score. The highest confidence score selects the final predicted rotational speed for the corresponding vibration sample.

CHAPTER IV

EXPERIMENTAL SETUP AND INSTRUMENTATION

4.1 UTCRS Laboratory Overview

The development of a machine learning algorithm requires sufficient data for analysis, training, and testing. Researchers at the UTCRS conduct bearing research using custom-built test rigs. The test rigs are designed to replicate field service bearing operation conditions under controlled load and speed settings. The laboratory facility includes two types of dynamic bearing test rigs namely, a single-bearing tester (SBT) and a four-bearing tester (4BT), equipped with load, temperature, and accelerometer sensors implemented onto custom-machined bearing adapters.

The bearings were generally subjected to two loading conditions, representing a fully-loaded rail car and an unloaded rail car, during laboratory testing. Fully-loaded (100% load) rail car class F and K bearings operate under the Association of American Railroads (AAR) suggested load capacity of 34,400 lbs (153 kN) whereas an unloaded railcar bearing experiences approximately 17% of this load capacity, or 5,848 lb (26 kN). Figure 18 shows a schematic diagram of the 4BT test axle setup and sensor placements. Vibration data acquired from top-loaded bearings (bearing 2 and 3 on the 4BT as well as the test bearing on the SBT) was used in this study as these bearings are more representative of the loading conditions bearings experience in rail revenue service. Figure 19 shows the SBT (left) and 4BT (right).

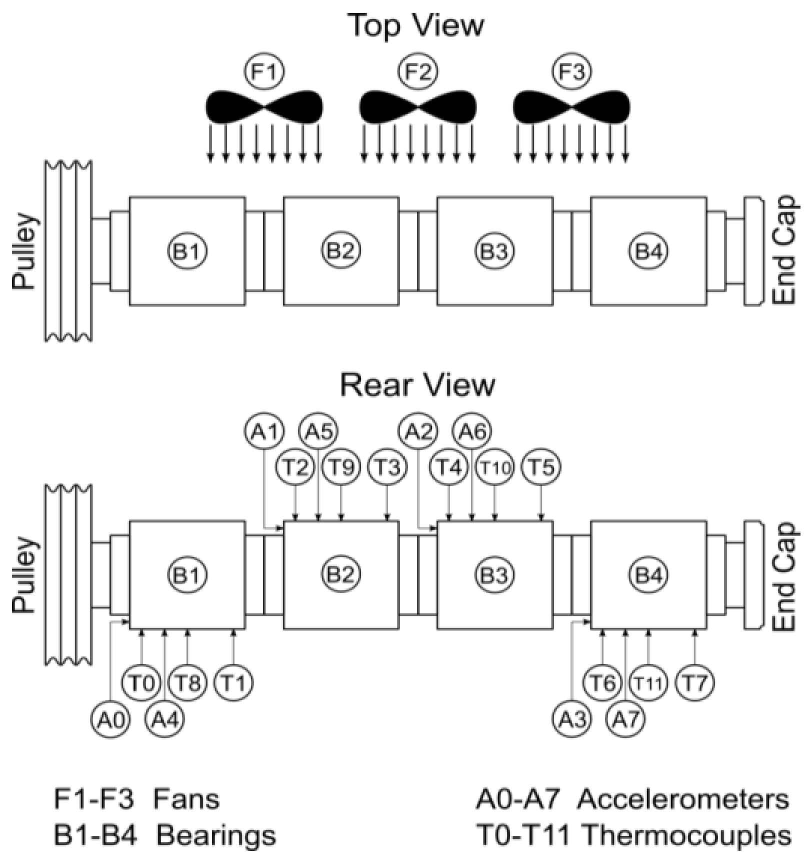

Figure 18: Four bearing test axle setup and instrumentation diagram.

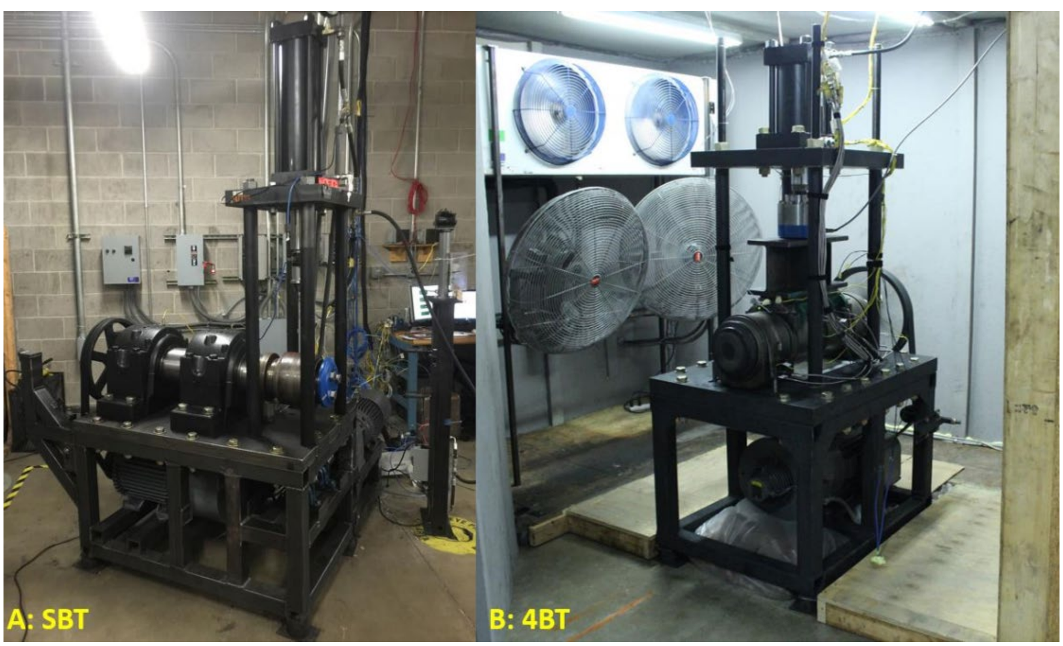

Figure 19: A) single bearing tester (SBT), and B) four bearing tester (4BT).

4.2 Bearing Test Rigs

The test rigs are individually powered by a 30 hp (22 kW) electric motor that is controlled by a variable frequency drive (VFD). These motors are connected to the test axle via a pulley-belt system. The VFD controls the axle rotation speed, simulating track speeds up to 85 mph (137 km/h) using a standard 36-inch wheel. Table 2 lists the most common simulated track speeds used during laboratory experiments.

Table 2: Common testing axle speeds and equivalent track speeds.

Axle Speed (rpm)	**234**	**280**	**327**	**374**	**420**	**467**	**498**	**514**	**560**	**618**	**700**	**796**
Track Speed (mph)	25	30	35	40	45	50	55	60	65	70	75	85
Track Speed (km/h)	40	48	56	64	72	80	85	89	97	106	121	137

Hydraulic cylinders are mounted above each test rig and can apply up to 150% of the AAR bearing rated load capacities. These hydraulic cylinders are regulated by specially-designed load controllers, capable of maintaining the applied bearing load to within 1% of the desired load. The 4BT test axle is supported by the two bottom-loaded bearings at the ends of the axle. The SBT test axle supports the cantilevered test bearing through the use of two consecutively placed SKF pillow block bearings to more accurately mimic field service conditions. In addition to simulating the railcar weight, the SBT can also apply lateral loading, simulating turns or wheel hunting, and impact loading, simulating wheel flats or rail defects. Figure 20 displays the features of the SBT.

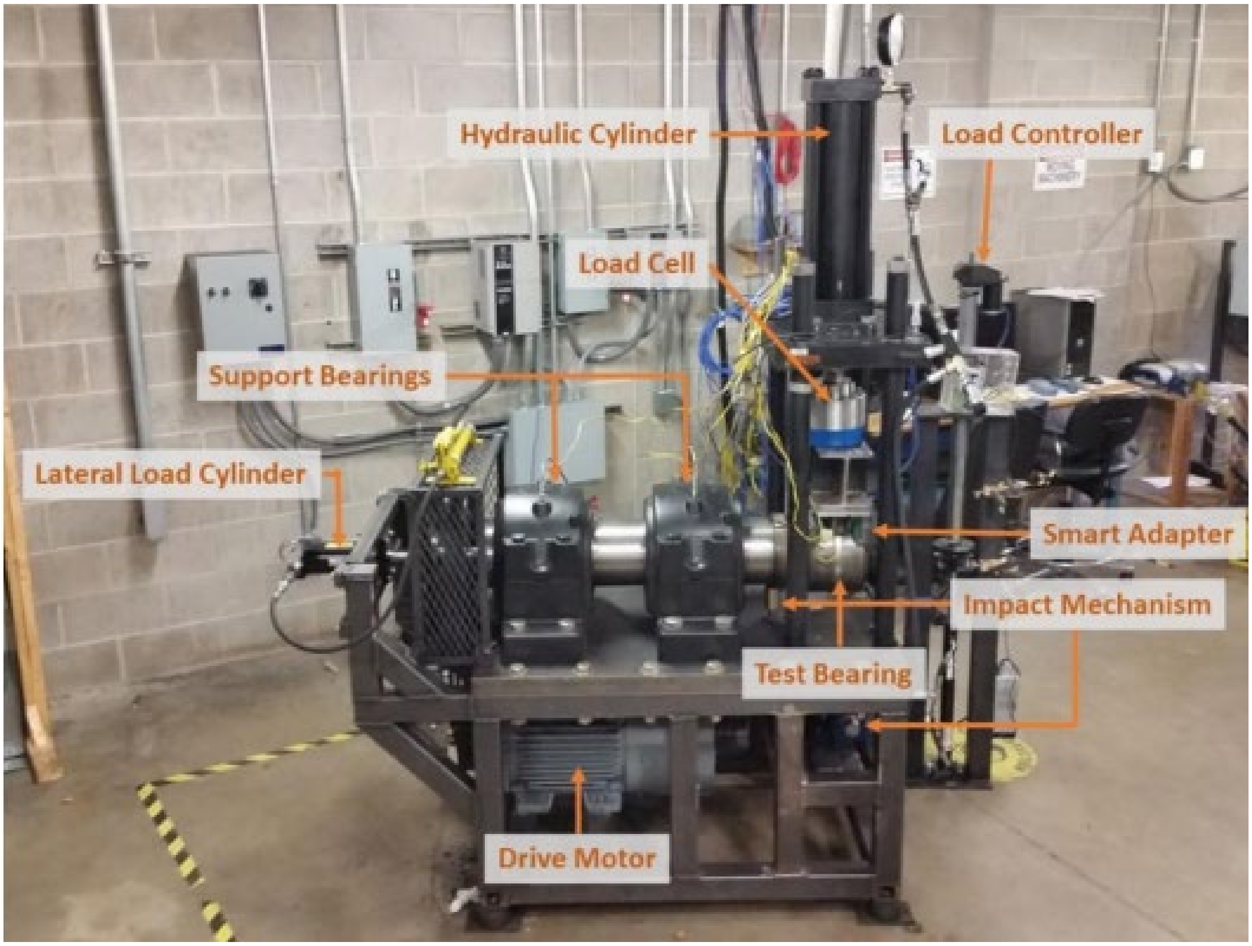

Figure 20: UTCRS single bearing tester (SBT) features.

4.3 Instrumentation

Vibration signatures are the most relevant feature to extract speed. The vibration data is collected using MEMS accelerometers, which have a measuring range of 100 g, mounted on the bearing adapter, as shown in Figure 7. These accelerometers are used alongside a data acquisition (DAQ) system that is sent to a central processing unit. The DAQ system uses a NI cDAQ-9174 chassis, NI 9215 module, NI 9239 DAQ module, and NI LabVIEW that collected these accelerometer measurements. These measurements are taken every 10 minutes for 16 seconds at a sampling rate of 5.12 kHz; thus, over 81,000 datapoints of accelerometer data is retrieved over the span of 16 seconds.

4.4 Software and Computational Environment

All signal processing, feature extraction, scoring, and speed-estimation algorithms were performed using MATLAB R2022b [14]. The analyses were executed on a dedicated workstation running Windows 11, equipped with a 12th-generation Intel® Core™ i7-12700 processor, 16 GB of RAM, and 512 GB of SSD storage. The workstation includes dual NVIDIA T1000 GPUs, which supports accelerated computation for high-volume vibration data processing. The signal processing, statistics, and machine learning toolboxes provided by MATLAB were used extensively throughout the development of the feature-extraction algorithm. This computational setup provided sufficient performance and stability for handling high-frequency accelerometer data and executing a full multi-stage speed approximation pipeline.

CHAPTER V

RESULTS AND DISCUSSION

5.1 Validation Experiments and Operating Conditions

Two experiments, one containing a cup defect and the other containing a cone defect, serve as the benchmark dataset for assessing algorithm performance. Experiment 181A and Experiment 177R feature bearings with a cone defect and a cup defect, respectively. The experiments were conducted under forty-four operating conditions, representing eleven speeds from Table 2, ranging from 234 rpm through 700 rpm, at unloaded and fully loaded conditions for cup and cone defective bearings. Section 5.2 will cover the algorithm performance of the forty-four operating conditions. Additionally, the algorithm was evaluated across three representative speed ranges in Sections 5.3 and 5.4: low-speed (234 rpm and 327 rpm), mid-speed (420 rpm and 560 rpm), and high-speed (618 rpm and 700 rpm) conditions. These speeds represent distinct operating environments that affect vibration amplitude, noise production, and defect modulation strength.

5.2 Aggregate Algorithm Performance

The aggregate results were analyzed across forty-four operating conditions and six filter-envelope combinations per experiment to evaluate the performance of the speed-extraction algorithm. The scoring metrics were calculated as described in Section 2.2 evaluating the speed prediction of each filter-envelope. This section provides an overview of the speed prediction accuracy for each method, independent of defect type and operating conditions. Table 3 lists the aggregate performance for Experiment 181A and 177R across all loading conditions and eleven speed settings. The key metrics analyzed were mean absolute error (MAE), mean relative error (MRE), mean score, mean composite score, and the percentage of cases that predict a speed less than or equal to a set percent error of the true speed. The number shots represents the amount of vibration acquisitions that support the MAE and MRE, providing context for the statistical reliability of the reported metrics. The mean score reported in Table 3 represents the average of the error-based metrics across all shots, including harmonic errors. Lower mean score values indicate better performance due to the score being formulated as an error measurement. The mean composite score is like the mean score, however it accounts for the penalties that were mentioned in Section 2.3.1. Lower composite score values again indicate a superior performance.

Table 3: Aggregate performance across all experiments and cases

Filter	Transform	Shots	Mean Absolute Error	Mean Relative Error	Cases ≤ 1% error [%]	Cases ≤ 5% error [%]	Cases ≤ 10% error [%]	Mean Score	Mean Composite Score
Wavelet	HIL	681	157	0.33	2.5	13	40	80	0.84
Wavelet	TEO	681	154	0.34	1.9	13	43	76	0.94
Lowpass	HIL	681	129	0.30	3.8	17	40	96	0.92
Lowpass	TEO	681	129	0.30	2.2	17	63	58	0.26
Bandpass	HIL	681	166	0.35	0.9	8.5	27	113	0.74
Bandpass	TEO	681	144	0.30	1.3	15	40	58	0.56

The mean relative error across all scenarios ranged from 0.30 to 0.35, where lowpass-HIL, lowpass-TEO, and bandpass-TEO output the lowest MRE of 0.30. Among the evaluated methods, the lowpass-TEO combination achieved the highest percentage of correct speeds within ±10% of the true speed outputting a value of 63%. This is followed by wavelet-TEO at 43% then both bandpass-TEO and lowpass-HIL at 40%.

The bandpass-TEO and lowpass-TEO combinations produced the lowest mean scores at 58. This indicates that those two combinations demonstrated better alignment between the observed peaks and the harmonic locations. Lowpass-TEO also achieved the lowest composite score of 0.26, consistent with its highest percentage of cases within ±10% error. Based on these metrics, the lowpass-TEO was identified as the most accurate filter-envelope combination. The following sections examine the performance across the three speed ranges to assess the strengths and limitations of each filter-envelope combination under varying operating conditions.

5.3 Results for Bearing with a Defective Cone (Exp. 181A)

Closer examination of the obtained results revealed that the performance of each filter-envelope combination was dependent on operating condition. A more detailed analysis is conducted to investigate the different behavioral trends of the individual filter-envelope combinations. This section quantifies algorithm performance as a function of rotational speed and load to understand how the defect-induced vibrations, noise levels, and signal modulations affect speed prediction accuracy for bearings containing a defective cone. The evaluation uses data from Experiment 181A. The results are presented using multiple performance metrics that enable consistent comparison of the filter-envelope combinations across operating conditions. The moniker of low, mid, and high speeds are relative to the laboratory speed settings rather than field operating conditions.

5.3.1 Low-Speed Conditions (234 rpm and 327 rpm)

Defect-induced modulations are often weak under low-speed conditions, resulting in low signal amplitudes that allow broadband noise to mask the fundamental frequencies and their harmonics. Table 4, Table 5, and Table 6 present the performance of each filter-envelope combination for bearings with defective cones under low-speed conditions, reported separately for the aggregated cases and loading conditions. This subsection examines two low-speed settings, 234 rpm and 327 rpm. This analysis first evaluates aggregated results at these low speed, followed by a separate analysis of each load condition.

Table 4: Algorithm aggregate performance at low-speed conditions (Exp. 181A)

Filter-Envelope	Shots	MAE (rpm)	MRE	Predictions within ±10% (%)	Mean Score	Mean Composite Score
Bandpass-HIL	74	39	0.15	53%	27	0.27
Bandpass-TEO	74	**29**	**0.11**	69%	**18**	**0.17**
Lowpass-HIL	74	55	0.21	41%	44	0.52
Lowpass-TEO	74	43	0.16	65%	42	0.49
Wavelet-HIL	74	43	0.15	65%	49	0.40
Wavelet-TEO	74	37	0.14	**72%**	36	0.31

Table 5: Low-speed results at 17% load (Exp. 181A)

Filter-Envelope	Shots	MAE (rpm)	MRE	Predictions within ±10% (%)	Mean Score	Mean Composite Score
Bandpass-HIL	37	33	0.13	70%	27	0.27
Bandpass-TEO	37	28	0.11	76%	16	0.15
Lowpass-HIL	37	52	0.19	57%	44	0.53
Lowpass-TEO	37	46	0.17	62%	49	0.53
Wavelet-HIL	37	37	0.11	**84%**	42	0.27
Wavelet-TEO	37	35	0.12	78%	30	0.19

Table 6: Low-speed results at 100% load (Exp. 181A)

Filter-Envelope	Shots	MAE (rpm)	MRE	Predictions within ±10% (%)	Mean Score	Mean Composite Score
Bandpass-HIL	37	46	0.17	35%	27	0.28
Bandpass-TEO	37	31	0.11	62%	19	0.18
Lowpass-HIL	37	57	0.22	24%	43	0.51
Lowpass-TEO	37	39	0.15	**68%**	34	0.45
Wavelet-HIL	37	49	0.19	46%	56	0.53
Wavelet-TEO	37	39	0.16	65%	43	0.43

The aggregated results listed in Table 4 show that wavelet-TEO output the highest precision, with 72% of predictions falling within ±10% error. However, bandpass-TEO surpassed the wavelet-TEO in terms of accuracy as shown by the error-based results. Low-speed cases were then examined separately under unloaded and fully loaded conditions to better understand algorithm performance, as shown in Table 5 and Table 6. This analysis revealed that neither wavelet-TEO nor bandpass-TEO yielded the best results when the unloaded and fully loaded cases were evaluated individually. Looking at Table 5, the wavelet-HIL algorithm achieved the highest ±10% accuracy at 84%, followed by wavelet-TEO with 78% accuracy under unloaded conditions. The TEO combinations demonstrated the best performance under fully loaded conditions, as can be seen in Table 6. Higher loading conditions at low speeds degraded overall performance across all filter-envelope combinations.

5.3.2 Mid-Speed Conditions (420 rpm and 560 rpm)

Performances were analyzed at unloaded and fully loaded conditions for two mid speeds (420 rpm and 560 rpm). Table 7 summarizes the aggregate results across the two tested loading conditions, whereas Table 8 and Table 9 provide a more detailed evaluation of mid-speed performance at unloaded and fully loaded cases, respectively.

Table 7: Algorithm aggregate performance at mid-speed conditions (Exp. 181A)

Filter-Envelope	Shots	MAE (RPM)	MRE	Predictions within ±10% (%)	Mean Score	Mean Composite Score
Bandpass-HIL	113	86	0.19	62%	48	0.44
Bandpass-TEO	113	67	0.15	67%	31	0.28
Lowpass-HIL	113	64	0.14	71%	46	0.45
Lowpass-TEO	113	98	0.21	69%	78	0.75
Wavelet-HIL	113	61	**0.13**	80%	35	0.31
Wavelet-TEO	113	67	0.14	**83%**	32	0.16

Table 8: Mid-speed results at 17% load (Exp. 181A)

Filter-Envelope	Shots	MAE (rpm)	MRE	Predictions within ±10% (%)	Mean Score	Mean Composite Score
Bandpass-HIL	56	69	0.15	75%	46	0.42
Bandpass-TEO	56	59	0.13	84%	33	0.29
Lowpass-HIL	56	59	0.13	77%	45	0.43
Lowpass-TEO	56	98	0.21	70%	85	0.78
Wavelet-HIL	56	49	0.11	88%	33	0.25
Wavelet-TEO	56	62	0.13	**91%**	26	0.12

Table 9: Mid-speed results at 100% load (Exp. 181A)

Filter-Envelope	Shots	MAE (rpm)	MRE	Predictions within ±10% (%)	Mean Score	Mean Composite Score
Bandpass-HIL	57	103	0.22	49%	49	0.47
Bandpass-TEO	57	74	0.17	53%	28	0.26
Lowpass-HIL	57	68	0.15	68%	48	0.46
Lowpass-TEO	57	98	0.20	68%	71	0.72
Wavelet-HIL	57	73	0.16	72%	38	0.29
Wavelet-TEO	57	72	0.16	**75%**	36	0.14

Wavelet-TEO performed best with 83% of predictions within a ±10% error for the aggregate analysis, listed in Table 7. Table 8 shows that wavelet-TEO continues to be favorable with 91% of predictions falling within a ±10% error when analyzing unloaded cases, followed by the wavelet-HIL combination which outputs 88% of predictions within a ±10% error. Wavelet-TEO remained the most consistent performer between both loading conditions outputting 75% of predictions within a ±10%. The fully loaded cases summarized in Table 9 show an overall higher MRE in comparison to the unloaded cases listed in Table 8. This trend indicated that the algorithm performance had higher accuracy at unloaded cases.

5.3.3 High-Speed Conditions (618 rpm and 700 rpm)

Signal amplitudes and modulations resulting from the presence of defects on the bearing raceways are often found to be greater at high-speed settings. However, these defect frequencies may be masked by broadband noise brought about by the speed setting and the dynamic interactions between rolling elements, raceways, and the cage. The performance of the filter-envelope combinations for two high speeds (618 rpm and 700 rpm) are evaluated in Table 10, Table 11, and Table 12. The aggregate algorithm performance was evaluated in Table 10 across both unloaded and loaded conditions. Table 11 and Table 12 presents the evaluated performance for the unloaded and loaded conditions, respectively.

Table 10: Algorithm aggregate performance at high-speed conditions (Exp. 181A)

Filter-Envelope	Shots	MAE (RPM)	MRE	Predictions within ±10% (%)	Mean Score	Mean Composite Score
Bandpass-HIL	80	368	0.55	8.8%	280	0.52
Bandpass-TEO	80	319	0.48	7.5%	194	0.43
Lowpass-HIL	80	226	0.33	**51%**	151	0.25
Lowpass-TEO	80	250	0.37	43%	196	0.37
Wavelet-HIL	80	421	0.62	40%	41	0.11
Wavelet-TEO	80	367	0.54	49%	39	0.09

Table 11: High-speed results at 17% load (Exp. 181A)

Filter-Envelope	Shots	MAE (rpm)	MRE	Predictions within ±10% (%)	Mean Score	Mean Composite Score
Bandpass-HIL	40	250	0.39	18%	234	0.44
Bandpass-TEO	40	216	0.34	15%	147	0.31
Lowpass-HIL	40	202	0.29	**63%**	181	0.27
Lowpass-TEO	40	236	0.34	48%	210	0.32
Wavelet-HIL	40	451	0.66	43%	40	0.11
Wavelet-TEO	40	415	0.61	55%	41	0.10

Table 12: High-speed results at 100% load (Exp. 181A)

Filter-Envelope	Shots	MAE (rpm)	MRE	Predictions within ±10% (%)	Mean Score	Mean Composite Score
Bandpass-HIL	40	486	0.71	0%	326	0.61
Bandpass-TEO	40	423	0.62	0%	241	0.56
Lowpass-HIL	40	250	0.36	40%	122	0.23
Lowpass-TEO	40	263	0.39	38%	181	0.42
Wavelet-HIL	40	391	0.58	38%	42	0.11
Wavelet-TEO	40	320	0.47	**43%**	36	0.08

Table 10 shows that lowpass-HIL and wavelet-TEO output the highest precision with 51% and 49% of predictions falling within ±10% error, respectively. Lowpass-HIL produced the lowest MRE of 0.29 and the highest frequency of accurate predictions, with 63% of estimates falling within ±10% error, as shown in Table 11. Although wavelet-TEO outperformed lowpass-HIL in terms of precision, the lower MRE of 0.36 indicated higher accuracy from lowpass-HIL at fully loaded conditions, as can be seen in Table 12. Lowpass-HIL demonstrated the best performance over high-speed settings.

5.3.4 Comparison Across Speed Ranges

The accuracy comparison between low-, mid-, and high-speed conditions can be deduced from the average output of the MRE between the six filter-envelope combinations. The average MRE for Table 4, Table 7, and Table 10 are 0.15, 0.16, and 0.48, respectively, which indicates an inverse proportional relationship between speed and accuracy. The precision of the algorithms is comparable between low and mid speeds, but decreases at high speeds as exhibited by the change in percentage of predictions within ±10% error.

5.4 Results for Bearings with a Defective Cup (Exp. 177R)

This section examines filter-envelope performance on a cup defective bearing using data from Experiment 177R. The three speed settings used in section 5.3 are utilized for an analysis done over the aggregate and individually assessed performance across two load conditions (unloaded and fully loaded). The following subsections present a comparative analysis of the filter-envelope combinations to characterize performance trends across these operating ranges.

5.4.1 Low-Speed Conditions (234 rpm and 327 rpm)

This section covers the performance of the speed-extraction filter-envelope combinations at low-speed (234 rpm and 327 rpm) for a cup defect. Table 13 covers the aggregate performance across unloaded and fully loaded conditions, whereas Table 14 and Table 15 present the evaluated performance for unloaded and fully loaded cases, respectively.

Table 13: Algorithm aggregate performance at low-speed conditions (Exp. 177R)

Filter-Envelope	Shots	MAE (RPM)	MRE	Predictions within ±10% (%)	Mean Score	Mean Composite Score
Bandpass-HIL	74	48	0.16	49%	28	0.28
Bandpass-TEO	74	45	0.15	**58%**	27	0.27
Lowpass-HIL	74	74	0.25	32%	63	0.72
Lowpass-TEO	74	69	0.23	41%	67	0.75
Wavelet-HIL	74	51	0.17	47%	48	0.39
Wavelet-TEO	74	48	0.16	57%	49	0.34

Table 14: Low-speed results at 17% load (Exp. 177R)

Filter-Envelope	Shots	MAE (rpm)	MRE	Predictions within ±10% (%)	Mean Score	Mean Composite Score
Bandpass-HIL	37	42	0.14	57%	26	0.28
Bandpass-TEO	37	44	0.15	**62%**	27	0.26
Lowpass-HIL	37	78	0.26	30%	64	0.74
Lowpass-TEO	37	72	0.24	38%	66	0.75
Wavelet-HIL	37	45	0.15	57%	43	0.35
Wavelet-TEO	37	49	0.16	49%	47	0.33

Table 15: Low-speed results at 100% load (Exp. 177R)

Filter-Envelope	Shots	MAE (rpm)	MRE	Predictions within ±10% (%)	Mean Score	Mean Composite Score
Bandpass-HIL	37	54	0.18	41%	30	0.29
Bandpass-TEO	37	47	0.16	**54%**	28	0.27
Lowpass-HIL	37	70	0.24	35%	61	0.69
Lowpass-TEO	37	66	0.22	43%	68	0.74
Wavelet-HIL	37	55	0.18	38%	53	0.43
Wavelet-TEO	37	48	0.16	49%	51	0.34

Table 13 shows that bandpass-TEO demonstrated the best performance with a precision of 58% for predictions within ±10% error and an MRE of 0.15. Table 14 shows that, in unloaded conditions, the bandpass-TEO remained the best performing algorithm with an MRE of 0.15 and a precision of 62% for predictions within ±10% error. For the fully loaded conditions, the bandpass-TEO remains the best performer with an MRE of 0.16 and a precision of 54% for predictions within ±10% error, as can be seen in Table 15.

5.4.2 Mid-Speed Conditions (420 rpm and 560 rpm)

An evaluation of the filter-envelope performance was conducted on a cup defective bearing for two mid-speed conditions (420 rpm and 560 rpm). The aggregate performance is evaluated in Table 16, while Table 17 and Table 18 present the evaluation of filter-envelope performance for unloaded and fully loaded conditions, respectively.

Table 16: Algorithm aggregate performance at mid-speed conditions (Exp. 177R)

Filter-Envelope	Shots	MAE (RPM)	MRE	Predictions within ±10% (%)	Mean Score	Mean Composite Score
Bandpass-HIL	113	96	0.21	60%	47	0.43
Bandpass-TEO	113	74	0.17	67%	33	0.29
Lowpass-HIL	113	70	0.15	64%	56	0.59
Lowpass-TEO	113	103	0.22	58%	79	0.78
Wavelet-HIL	113	66	0.14	71%	51	0.39
Wavelet-TEO	113	62	0.13	**77%**	43	0.23

Table 17: Mid-speed results at 17% load (Exp. 177R)

Filter-Envelope	Shots	MAE (rpm)	MRE	Predictions within ±10% (%)	Mean Score	Mean Composite Score
Bandpass-HIL	56	69	0.15	70%	45	0.41
Bandpass-TEO	56	69	0.16	71%	38	0.33
Lowpass-HIL	56	60	0.13	77%	52	0.54
Lowpass-TEO	56	94	0.20	64%	67	0.66
Wavelet-HIL	56	55	0.12	80%	48	0.37
Wavelet-TEO	56	61	0.13	**84%**	38	0.19

Table 18: Mid-speed results at 100% load (Exp. 177R)

Filter-Envelope	Shots	MAE (rpm)	MRE	Predictions within ±10% (%)	Mean Score	Mean Composite Score
Bandpass-HIL	57	123	0.27	53%	49	0.45
Bandpass-TEO	57	80	0.17	63%	28	0.26
Lowpass-HIL	57	81	0.17	61%	60	0.59
Lowpass-TEO	57	111	0.24	53%	79	0.78
Wavelet-HIL	57	77	0.17	63%	57	0.43
Wavelet-TEO	57	64	0.14	**68%**	45	0.25

The wavelet-TEO remained the top performer between both unloaded and fully loaded conditions, resulting in the best aggregate performance, as shown in Table 16. At unloaded conditions, the precision of prediction was found to be 84% within ±10% error, while at fully loaded conditions, this precision decreased to 68%. This trend suggests that unloaded conditions are more favorable as the signal amplifications of defects are more prominent.

5.4.3 High-Speed Conditions (618 rpm and 700 rpm)

Cup defects excite outer-race frequencies that can be overshadowed by wheel-rail resonance and structural vibrations at higher speeds, making it considerably more difficult to extract speed. Table 19 covers the aggregate performance across unloaded and fully loaded conditions, while Table 20 and Table 21 present the results for unloaded and fully loaded conditions for cup defects, respectively.

Table 19: Algorithm aggregate performance at high-speed conditions (Exp. 177R)

Filter-Envelope	Shots	MAE (RPM)	MRE	Predictions within ±10% (%)	Mean Score	Mean Composite Score
Bandpass-HIL	80	390	0.59	6.3%	296	0.55
Bandpass-TEO	80	348	0.53	6.3%	220	0.51
Lowpass-HIL	80	258	0.39	**40%**	157	0.26
Lowpass-TEO	80	262	0.39	35%	208	0.40
Wavelet-HIL	80	464	0.70	31%	44	0.11
Wavelet-TEO	80	479	0.72	33%	47	0.12

Table 20: High-speed results at 17% load (Exp. 177R)

Filter-Envelope	Shots	MAE (rpm)	MRE	Predictions within ±10% (%)	Mean Score	Mean Composite Score
Bandpass-HIL	40	268	0.41	15%	215	0.41
Bandpass-TEO	40	253	0.39	15%	155	0.30
Lowpass-HIL	40	239	0.36	**55%**	212	0.32
Lowpass-TEO	40	217	0.33	50%	165	0.33
Wavelet-HIL	40	470	0.71	33%	38	0.10
Wavelet-TEO	40	499	0.75	30%	42	0.11

Table 21: High-speed results at 100% load (Exp. 177R)

Filter-Envelope	Shots	MAE (rpm)	MRE	Predictions within ±10% (%)	Mean Score	Mean Composite Score
Bandpass-HIL	40	512	0.77	0%	377	0.69
Bandpass-TEO	40	443	0.66	0%	273	0.65
Lowpass-HIL	40	277	0.41	25%	108	0.19
Lowpass-TEO	40	307	**0.46**	20%	216	0.48
Wavelet-HIL	40	418	0.60	**35%**	50	0.12
Wavelet-TEO	40	451	0.64	35%	42	0.09

The aggregate results demonstrate that lowpass-HIL consistently performed the best for cup defects with an MRE of 0.39 and a precision of 40% for predictions within ±10% error. In unloaded cases for lowpass-HIL the precision was found to be 55%, whereas the fully loaded cases demonstrated a precision of 25%.

5.4.4 Comparison Across Speed Ranges

The algorithm struggles at making predictions in high-speed settings more so than other speed ranges. The average MRE for Table 13, Table 16, and Table 19 are calculated to be 0.19, 0.17, and 0.55 representing results for low-, mid-, and high-speed conditions, respectively. In contrast to cone defects, the cup defect performance demonstrated a decrease in overall precision. It is shown in Section 5.4.1 through Section 5.4.3 that precision decreases as the speed increases.

5.5 Reliability Analysis of Speed Estimation for Early Defect Detection

A probability analysis was performed to quantify the likelihood of the proposed feature extraction algorithm to estimate the speed of a defective bearing, thereby enabling the correct speed to be input to the Level 2 algorithm developed by Montalvo and Gonzalez [6] [10]. The feature-extraction algorithm was specifically designed to be used on defective bearings to conduct a level 2 health assessment, implying that healthy bearings do not require the speed to be extracted. Early defect detection in this section is defined as the likelihood of obtaining a speed prediction that lies within a ±10% deviation from the true speed within four vibration acquisitions. These four vibration signature acquisitions, otherwise referred to as shots, represent 40 minutes of operation.

Vibration data was collected in 16-second shots every 10 minutes. Each shot was treated as a Bernoulli trial, where success was defined as a speed estimated within ±10% relative error. The empirical single-shot probability of a correct speed extraction is represented by Equation (36), where *k* represents the number of predictions that are accurate within ±10%.

$$P_{speed} = \frac{k}{n} \tag{36}$$

Furthermore, the probability of retrieving at least one correct speed prediction over *m* attempts is represented by Equation (37),

$$P_{at\ least\ one\ in\ m} = 1 - \left(1 - P_{speed}\right)^{m} \tag{37}$$

Where *m* is equal to the number of shots or opportunities to obtain the correct speed estimate.

The probability model provides a measure of how reliably the feature extraction algorithm can obtain at least one correct speed prediction within 40 minutes of operation ($m = 4$). Table 22 and Table 23 present the probability of obtaining at least one correct speed estimate within four shots for bearings containing either a defective cone or cup using data provided by Experiments 181A and 177R, respectively. These probabilities were calculated by using the best performing filter-envelope combination for each speed-load condition.

Table 22: Probability of early detection for cone defective bearings (Exp. 181A)

Speed Band	Load	Best Method	Shots	P_{speed}	$P_{at\ least\ 1\ in\ 4}$
Low (234–327 rpm)	17%	Lowpass–TEO	34	0.853	**1.000**
Low (234–327 rpm)	100%	Bandpass–TEO	40	0.650	**0.985**
Mid (420–560 rpm)	17%	Lowpass–TEO	40	1.00	**1.000**
Mid (420–560 rpm)	100%	Lowpass–TEO	40	0.800	**0.998**
High (618–700 rpm)	17%	Lowpass–TEO	40	0.625	**0.980**
High (618–700 rpm)	100%	Wavelet–TEO	40	0.600	**0.974**

Table 23: Probability of early detection for cup defective bearings (Exp. 177R)

Speed Band	Load	Best Method	Shots	P_{speed}	$P_{at\ least\ 1\ in\ 4}$
Low (234–327 rpm)	17%	Lowpass–TEO	40	0.475	**0.924**
Low (234–327 rpm)	100%	Lowpass–TEO	33	0.333	**0.802**
Mid (420–560 rpm)	17%	Bandpass–TEO	37	0.811	**0.999**
Mid (420–560 rpm)	100%	Lowpass–TEO	33	0.606	**0.976**
High (618–700 rpm)	17%	Lowpass–TEO	40	0.900	**1.000**
High (618–700 rpm)	100%	Lowpass–TEO	40	0.550	**0.959**

The probability of early defect detection is consistently high for cone defects exceeding 97%, as shown in Table 22. Feature extraction for bearings containing cup defects demonstrate a probability of early defect detection of at least 80.2%. These probability results are higher compared to the precision values presented in Section 5.3 and Section 5.4. This result can be explained by the fact that the probability analysis evaluates whether any of the six methods succeeded within the observation window, whereas the precision metric is based solely on the average performance of the six filter-envelope combinations. Since the algorithm proposes to evaluate all six methods simultaneously, a single successful method is sufficient to derive the speed input needed to run the Level 2 defect detection algorithm.

CHAPTER VI

CONCLUSIONS AND FUTURE WORK

This thesis developed and evaluated a vibration-based speed-extraction algorithm designed to support the UTCRS Level 2 defect detection framework for railroad tapered roller bearings. The algorithm reliably isolated fundamental defect frequencies and reverse-calculated rotational speed across a wide range of operating conditions by integrating signal processing techniques. These techniques included envelope extraction, harmonic pairwise peak analysis, and K-Means machine learning clustering. The algorithm was comprised of six filter-envelope combinations, that integrated wavelet, lowpass, and bandpass filtering with Hilbert (HIL) and Teager Energy Operator (TEO) envelopes to demodulate the vibration signature. These combinations extracted the fundamental defect frequencies. Results from controlled laboratory experiments on both inner (cone) and outer (cup) raceway defects demonstrated that individual filter-envelope combinations varied in performance across different operational settings. The multi-method framework ensures that at least one algorithm consistently estimates the operating rotational speed accurately, regardless of operating conditions. A probability analysis confirmed that the likelihood of obtaining a correct speed was generally above 90% for both cup and cone defects across various operating conditions using four shots of data (40 minutes of operation).

Future work should contribute to expanding experimental conditions and datasets to enable validation of energy-based confidence scoring. Additionally, further work is required to develop a classification logic capable of distinguishing between cup and cone defects when harmonic spacing alone does not uniquely determine defect type. Incorporating signal descriptors, deep-learning architectures, or probabilistic sensor-fusion methods may improve robustness of the algorithm under noisy vibration profiles. Ultimately, field deployment and long-duration testing on rail revenue service is essential for demonstrating the readiness of the multi-level onboard condition monitoring algorithm towards autonomous real-time defect detection and identification.

REFERENCES

[1] United States, Dept. of Transportation, "An Implementation Guide for Wayside," Federal Railroad Administration, Washington, DC, 2019.

[2] National Transportation Safety Board, "Norfolk Southern Railway Derailment and Hazardous Materials Release," East Palestine, OH, 2024.

[3] American Society of Civil Engineers, "2025 Infrastructure Report Card," 2025. [Online]. Available: https://infrastructurereportcard.org/wp-content/uploads/2025/03/Rail.pdf.

[4] Federal Railroad Administration, "Code of Federal Regulations," [Online]. Available: https://www.ecfr.gov/current/title-49/subtitle-B/chapter-I/subchapter-C/part-179/subpart-B/section-179.13.

[5] Association of American Railroads, Manual of Standards and Recommended Practices, Washington D.C.: The Association of American Railroads, 2023.

[6] J. Montalvo, C. Tarawneh and A. Fuentes, "Vibration-Based Defect Detection for Freight Railcar Tapered-Roller Bearings," in *2018 Joint Rail Conference*, Edinburg, Tx, 2018.

[7] C. Tarawneh, J. Aranda, V. Hernandez, S. Crown and J. Montalvo, "An investigation into wayside hot-box detector efficacy and optimization," *International Journal of Rail Transportation,* vol. 8, no. 3, pp. 264-284, 2020.

[8] J. R. L. Cuanang, "Optimizing a Railroad Bearing Condition-Monitoring Algorithm for Use with an Onboard Wireless Low-Power Sensor Module," The University of Texas Rio Grande Valley, Edinburg, TX, 2020.

[9] K. Quaye, P. Xu, D. Dera, H. Foltz, C. Tarawneh and A. Diaz, "Feature Extraction From Vibration Signature Required From Railroad Bearing Onboard Condition Monitoring Sensor Modules," in *Proc. 2024 Joint Rail Conference*, Columbia, SC, USA, 2024.

[10] A. Gonzalez, "Development, optimization, and implementation of a vibration based defect detection algorithm for railroad bearings," ProQuest LLC, Ann Arbor, 2015.

[11] J. Pams, C. Tarawneh, D. Rocha, B. Wilson, L. Cantu and H. Alkhaldi, "Optimized Vibration-Based Health Metrics for Freight Rail Bearings," in *2024 Joint Rail Conference*, Columbia, South Carolina, USA, 2024.

[12] C. Tarawneh, J. A. Kypuros, B. M. Wilson, T. W. Snyder, A. A. Fuentes and B. A. Gonzalez, "A Collaborative On-Track Field Test Conducted to Verify the Laboratory Findings on Bearing Temperature Trending," in *2009 Joint Rail Conference*, 2009.

[13] A. M. Ikotun, A. E. Ezugwu, L. Abualigah, B. Abuhaija and J. Heming, "K-means clustering algorithms: A comprehensive review, variants analysis, and advances in the era of big data," *Information Sciences,* vol. 622, pp. 178-210, 2023.

[14] The MathWorks, Inc., "MATLAB, Version R2022b," Natick, MA, USA, 2022.

[15] I. L. Alvarado, Defect Detection in Railroad Tapered-Roller Bearings Using Vibration Analysis Techniques, Ann Arbor: ProQuest LLC, 2013.

[16] S. M. Martinez, "Vibration-Based Machine Learning Models for Condition Monitoring of Railroad Rolling Stock," 2023.

[17] U.S. Department of Transportation (USDOT), "Steps Forward for Freight Rail Industry Safety," U.S. Department of Transportation (USDOT), 21 February 2023. [Online]. Available: https://www.transportation.gov/briefing-room/us-department-transportation-fact-sheet-steps-forward-freight-rail-industry-safety.

APPENDIX

APPENDIX

CONFIDENCE-ERROR CORRELATION ANALYSIS

A correlation analysis was performed between the confidence values and the calculated speed errors to evaluate whether the confidence scores reflect the reliability of the speed predictions. The Pearson correlation coefficient (ρ) was used to quantify the relationship between the confidence score and the error as shown in Equation (38). High confidence scores correspond to low errors, implying reliable predictions.

$$\rho = \frac{\sum_{i=1}^{N}(X_i - \bar{X})(Y_i - \bar{Y})}{\sqrt{\sum_{i=1}^{N}(X_i - \bar{X})^2}\sqrt{\sum_{i=1}^{N}(Y_i - \bar{Y})^2}} \tag{38}$$

In Equation (38), X_i represents the confidence score of the ith trial, Y_i represents the relative error of the same trial, both $\bar{X}$ and $\bar{Y}$ are their respective means, and ρ is the Pearson correlation coefficient ranging from -1 to 1.

A correlation study was performed between the confidence values for each filter-envelope combination and their corresponding speed estimation errors to gauge the reliability. Table 24 displays the confidence-error correlations using Pearson correlation values for each filter-envelope combination output by Equation (38). A positive correlation represents an error indication, and a negative correlation demonstrates the desired trend between high confidence score and low accuracy errors. It should be noted that the following confidence score behaved as an error-indicator metric rather than as a true measure of prediction reliability.

Table 24: Confidence-error correlations using Pearson correlation values

Filter	Transform	$\rho_{abs\ err}$	$\rho_{rel\ err}$
Bandpass	Hilbert	0.54	0.24
Bandpass	TEO	**0.61**	**0.40**
Lowpass	Hilbert	0.38	0.10
Lowpass	TEO	**0.73**	**0.60**
Wavelet	Hilbert	0.55	0.35
Wavelet	TEO	0.59	0.36

The results found in Table 24 indicate that all confidence scores for the filter-envelope methods give a positive correlation between absolute and relative error. As mentioned earlier, the structure of the scoring methods behaves more like an error indicator rather than a measure of estimation. This means that higher confidence levels are generally associated with poor speed estimations, rather than inference on the reliability. Lowpass-TEO and bandpass-TEO demonstrate the strongest positive correlations, suggesting that their confidence values increase most sharply as errors increase. Additionally, the lowpass-HIL shows a weak correlation and indicates a non-reliable confidence score as it is close to zero.

VITA

Diego Cantu attended Vanguard Rembrandt Secondary and graduated in 2019. He received his Bachelor of Science in Mechanical Engineering from the University of Texas-Rio Grande Valley (UTRGV) in May 2023. He furthered his education at UTRGV and earned his Master of Science in Mechanical Engineering in December 2025. During his undergraduate studies he began conducting research in the machine-learning sector at the National Science Foundation CREST Center for Multidisciplinary Research Excellence in Cyber-Physical Infrastructure Systems (CREST-MECIS), where he contributed to a U.S. Department of Homeland Security-sponsored research project focused on machine-vision for swarm robotics. He later served as AI graduate research assistant under the CREST-MECIS center where he conducted research on feature-extraction using vibration-signature of railway bearings. He can be reached by email at diegocantu894@gmail.com